A Regularised Anisotropic Elastoplastic Damage and Viscoplastic Model and Its Hydromechanical Application to a Meuse/Haute-Marne URL Drift

Mountaka Souley, E.-D. Coarita-Tintaya, M.-N. Vu, F. Golfier, G. Armand, M. Laviña, A. Idiart

▶ To cite this version:

Mountaka Souley, E.-D. Coarita-Tintaya, M.-N. Vu, F. Golfier, G. Armand, et al.. A Regularised Anisotropic Elastoplastic Damage and Viscoplastic Model and Its Hydromechanical Application to a Meuse/Haute-Marne URL Drift. Rock Mechanics and Rock Engineering, 2023, 10.1007/s00603-023-03563-1 . ineris-04276528

HAL Id: ineris-04276528
https://ineris.hal.science/ineris-04276528

A regularised anisotropic elastoplastic, damage and viscoplastic model and its hydromechanical application to a Meuse/Haute-Marne URL drift

M. Souley[a*], E.-D. Coarita-Tintaya[a,b], M.-N. Vu[c], F. Golfier[b], G. Armand[c], M. Laviña[d] and A. Idiart[d]

[a] National Institute for Industrial Environment and Risks (Ineris), Nancy, France

[b] University of Lorraine (UL), CNRS, GeoRessources Laboratory, Nancy, France

[c] French National Radioactive Waste Management Agency (Andra), Châtenay-Malabry, France

[d] Amphos 21 Consulting, Barcelona, Spain

*Corresponding author - E-mail: Mountaka.Souley@ineris.fr

Abstract

Clay formations are one of the options currently being considered for the storage of radioactive wastes worldwide. In France, the National Radioactive Waste Management Agency (Andra) operates the Meuse/Haute-Marne Underground Research Laboratory in the Callovo-Oxfordian (COx) clay formation to assess the feasibility and safety of an industrial radioactive waste repository. A good level of understanding of the thermo-hydro-mechanical behaviour of the host rock is paramount for the safety assessment.

A new anisotropic elastoplastic, damage and viscoplastic model is proposed to describe the hydromechanical behaviour of the COx claystone based on a large dataset of experimental evidence. The model is based on the Hoek and Brown criterion and considers recent findings of the COx hydromechanical behaviour. The key mechanisms considered are: plastic strain hardening prior to reaching the peak strength, a post-peak behaviour characterized by strain softening in the frame of continuum damage mechanics, and a residual stage represented by a perfectly plastic behaviour. Time-dependent deformations are also included based on a creep model, which in this work is coupled with damage. The proposed model was implemented with a regularisation scheme based on the non-local implicit gradient in Comsol Multiphysics® with the purpose of performing THM modelling (1D, 2D and 3D) in the framework of the Cigéo project. The numerical implementation is first validated based on several simulations of creep tests at different deviatoric stress and triaxial compression tests at different confining pressure and angle between the loading direction and the bedding, α*. Then, the GCS drift hydromechanical behaviour is simulated considering transverse isotropic conditions. It is shown that the model is capable of reproducing the measured peak of pore pressure in sensors near the GCS wall as well as the drift convergence. Importantly, the predicted extent of damaged zones around the drift is consistent with the in situ observations. The impact of damage on the time-dependent behaviour and the permeability was investigated numerically. It was found that the magnitude and anisotropy of drift convergence and the pore pressure drop are sensitive to this coupling and the best agreement was obtained when this effect was taken into account. Finally, the performance of the regularisation scheme is demonstrated with a set of simulations of the drift with different mesh refinement. It is concluded that the proposed model captures the key features of the hydromechanical behaviour of the COx claystone.*

Highlights

- An advanced constitutive model that takes into account the recent findings on the key mechanisms of deformation and failure of COx claystone is proposed.
- Strain hardening/softening, Anisotropic elasticity and plasticity, Damage described in the framework of CDM and Time-dependent behaviour of COx claystone are considered.
- The effect of damage and shear fracturation on the transport and viscous properties are also addressed in the model.
- The model with a regularisation scheme is implemented in Comsol Multiphysics®, which allows several physics to be considered, then to perform 1D, 2D and 3D THMC modellings.
- The operational nature of the proposed model is successfully evidenced on the GCS drift of M-HM URL for which the in situ observations are the most challenging to reproduce.

Keywords

Constitutive model; anisotropy; elastoplasticity; damage; viscoplasticity; permeability changes; regularisation

1. Introduction

Within the perspective of deep geological radioactive waste disposal, the French National Radioactive Waste Management Agency (Andra) is conducting a research program that includes in situ experiments at the Meuse/Haute-Marne Underground Research Laboratory (MHM URL). The objectives of this URL are firstly to demonstrate the feasibility of constructing and operating a high-level and intermediate-level long-lived waste disposal facility, secondly to assess the safety of an industrial radioactive waste repository (Cigéo), and finally to optimize different components of Cigéo. A thorough scientific research program, including specific in situ experiments and laboratory tests, has been undertaken since 2000 to characterize and to understand the thermo-hydro-mechanical (THM) behaviour of the Callovo Oxfordian (COx) claystone (Armand et al. 2013, 2015, 2017a, b). In parallel, theoretical analyses, constitutive models and numerical modelling have been developed to describe the key THM processes expected to occur under repository conditions and various time scales (Seyedi *et al*. 2017, Pardoen and Collin 2017, Manica et al. 2021, etc.).

More specifically, understanding of the excavation-induced fractures zone (EFZ) around the galleries is crucial in the context of deep geological disposal of nuclear waste, as fractures can potentially act as migration pathways for radionuclides. Thus, part of the in situ investigations was devoted to their characterization around the drifts of the MHM URL, which has been essentially excavated following the two main directions of major (σ_H) and minor (σ_h) horizontal stresses (Armand et al. 2014). It has been shown that excavation at the main level of the MHM URL (-490 m) induces an EFZ around the drifts, which according to Armand et al. (2014) can be divided into two sub-domains. A connected fracture zone (CFZ) where both extensional and shear fractures co-exist, with an extension of about 0.4xD from the drift wall (D is the drift diameter) in the direction of the initial minor principal stress of the drift section. A more extended discrete fractured zone (DFZ) between the CFZ and the intact rock with only shear fractures, is additionally formed. The average extension of the DFZ is about 0.8xD from drift wall in the direction of the initial minor principal stress. In the direction of major principal stress of the drift section, very limited or no CFZ has been reported, and the maximum DFZ extent is 0.5xD. The CFZ is characterized by a high fracture density that significantly affects permeability (e.g., Tsang et al. 2005). An increase of up to 3 to 4 orders of magnitude compared to the intrinsic permeability of the intact rock has been reported in the CFZ, mainly attributed to the hydraulic transmissivity of the induced fractures (de la Vaissière et al 2015). In turn, the increase in permeability in the DFZ remains moderate. Permeability measurements during triaxial compression tests show only slight changes during the elastic and the plastic hardening stages and a drastic increase in the post-peak stage. The latter is attributed to the development of cracks and shear bands. Anisotropies of CFZ and DFZ extents have been observed systematically around all the galleries of the main level: whether they are parallel to σ_h, as in the GED drift (which is expected because of the high initial stress anisotropy in its section) or parallel to σ_H, such as the GCS drift while the initial stress state is almost isotropic in the drift section. Consequently, anisotropies in drift convergence and pore pressure distribution have also been evidenced by field measurements (Armand et al. 2013, 2015, 2017a, b; Seyedi et al. 2017; Vu et al. 2020).

Due to the isotropic in situ stress state in the GCS drift section, the observed large anisotropies of DFZ and CFZ extension, convergences and pore pressure distributions around this drift are the most challenging to reproduce (Vu et al. 2020, Manica et al. 2021). Some of the in situ observations and measurements around the GCS drift parallel to σ_H are illustrated in Figure 1 which we will address later (at the main level, σ_H ~ 16.2 MPa, σ_h ~ 12.4 MPa, and σ_v ~ 12.7 MPa, Wileveau et al. 2007).

Since 2000, numerous campaigns of laboratory tests have been undertaken to characterize and understand the mechanical, hydromechanical and THM behaviour of the COx claystone. Based on these experimental results as well as on in situ evidences, several constitutive models have been developed for the COx claystone under saturated and unsaturated conditions. These are mainly phenomenological elastoplastic, elastoviscoplastic, viscoplastic and damage models (Hoxha *et al*. 2007, Bian *et al*. 2017, Cuvilliez *et al*. 2017, Souley *et al.* 2017, Trivellato et al. 2019), coupled elastoplastic and damage models (Chiarelli *et al.* 2003, Conil *et al.* 2004, Jia *et al.* 2009), anisotropic elastic or elastoplastic and viscoplastic models (Manica *et al*. 2017, 2021; Pardoen and Collin 2017, Yu *et al.* 2021) and anisotropic elastoplastic taking into account planes of weakness (Souley *et al*. 2022). Other types of models based on micromechanics (Yanqiu and Shao 2013) or discrete elements (Yao *et al.* 2017, Dinç and Scholtes 2018) have also been applied to COx claystone.

Strain localization in geomaterials has been extensively investigated experimentally (Desrues and Viggiani 2004), theoretically (Sulem 2010) and numerically (Sabet and de Borst 2019). It is well known that modelling of geomaterials exhibiting a strain-softening behaviour with continuous approaches leads to numerical solutions heavily dependent on the size of the mesh elements and sometimes to numerical instabilities. The post-peak regime is usually characterized by strain localization bands which thickness has been shown to depend on the mesh size (Pietruczack and Mroz 1981, de Borst and Mühlhaus 1992, Wu and Wang 2010, Sabet and de Borst 2019). This instability is due to the ill-posed mathematical problem that leads to convergence towards not physically sound solutions, and thus to a loss of uniqueness of the solution, i.e., ellipticity or hyperbolicity loss of the governing differential equations (Pietruczack and Mroz 1981, Aifantis, 1984, Read and Hegemier 1984, de Borst *et al.* 1993, Peerlings *et al.* 1996a,b, Valanis and Peters 1996, Lu et al. 2009; Summersgill et al. 2017, Sabet and De Borst 2019). One way to remedy this is to use regularisation methods. Regularisation methods are solved simultaneously with the constitutive law and incorporate a characteristic length that depends on the material (Patzák and Jirásek 2004) to prevent localization of strain into an arbitrarily small volume (Jirásek 2007). These models are typically non-local, in the sense that the value of the regularised variable at a given point depends on the values in a neighbouring region defined by the characteristic length. Regularisation techniques can be broadly divided into non-local integral models (Peerlings et al. 1996a, Bazant et al. 1984, Pijaudier-Cabot and Bazant 1987, Bazant and Jirasek 2002, Summersgill *et al.* 2017, Lu et al. 2009 or Mánica et al. 2018) and differential or gradient-enhanced models (Aifantis 1984; de Borst and Mühlhaus 1992; Peerlings et al. 1996b, Miehe et al. 2013). The latter can be implemented in either the explicit or implicit forms (Peerlings et al. 1996, Askes and Sluys 2002, Simone 2007). The phase field method is another approach to model strain localization and has proved particularly well suited to study localization and coalescence of cracks in brittle materials (Zhou et al. 2018, 2019; Yu et al. 2021).

Similar to other quasi-brittle geomaterials, the mechanical behaviour of COx claystone is characterized by the initiation, growth and coalescence of microcracks and/or the formation of shear bands in the post-peak regime (Bésuelle and Lanata 2014; Desbois et al. 2017; Zhang 2016, Zhang et al. 2019). Appropriate modelling of this material behaviour requires the use of a regularisation technique to overcome the problem of mesh dependence and thus to better represent the development of the EFZ around the structures of MHM URL. Recently, Manica et al. (2021) regularised their rheological model by a non-local integral formulation in the finite element code PLAXIS, Pardoen and Collin (2017) used the local second gradient in the finite element code LAGAMINE and Yu *et al.* (2021) regularised their model by using the phase field method.

The present paper is a part of ongoing collaborative scientific research on the development of advanced constitutive models for COx claystone behaviour and robust numerical tools suitable for the THMC modelling in the Cigéo project in 1D, 2D and 3D. The objective of this paper is therefore to develop an advanced constitutive model that takes into account the key mechanisms of deformation and failure of COx claystone. This model needs to be available in an industrial software for future THM or THMC modelling in the framework of the Cigéo project.

Based on available experimental data, an anisotropic elastoplastic, damage and viscoplastic model is proposed to describe the hydromechanical behaviour of the COx claystone. The model considers state-of-the-art knowledge of the mechanical and hydromechanical behaviour of COx claystone and focuses on the key mechanisms. The pre-peak behaviour is characterized by plastic hardening with a non-associated flow rule. Damage starts in the post-peak (softening) regime, which is described in the framework of Continuum Damage Mechanics (CDM). This is followed by a residual phase represented by perfect plasticity. Brittle behaviour under low confining pressure (σ_3) becomes gradually ductile with the increase of σ_3. The anisotropic character of the model stems from several laboratory tests performed on COx that indicate minimum compressive strengths at about 30-45° to the bedding plane. Maximum values are reached in the direction parallel or perpendicular to bedding. Here, the peak strength and elastic limit are assumed to have the same evolution with respect to the angle between the loading direction and the bedding, α. The model also considers time-dependent deformations based on the isotropic Lemaître's model as suggested by creep tests. The creep strain depends on damage and shear fracture (Souley et al. 2017). The proposed model was implemented in the commercial code, Comsol Multiphysics®, which allows several physics to be considered.

This paper is organised as follows. Section 2 gives an overview of the main characteristics of COx claystone behaviour (transversely isotropic elastic, hardening, softening and residual plastic strains, brittle-ductile transition, mechanical time-dependent behaviour, hydromechanical coupling, etc.) evidenced by the laboratory investigations as well as the constitutive equations governing these mechanisms. Section 3 presents the selected regularisation method for the internal variables (damage and shear plastic strain). Section 4 discusses the numerical implementation of the proposed model in Comsol Multiphysics® and then validates the model implementation through simulations on simple loading paths. The operational and practical character of the model is demonstrated in Section 5 based on the GCS drift. This study case concerns one of the main challenges of the application of advanced constitutive models, which is to reproduce all the relevant in situ observations and measurements around the drift. Conclusions and perspectives are finally drawn in Section 6.

2. Experimental evidences on the COx claystone behaviour

The hydromechanical behaviour of COx claystone has been studied experimentally by several authors (Chiarelli et al. 2003, Zhang and Rothfuchs 2004, Hoxha et al. 2007, Hu et al. 2014, Menaceur et al. 2015, Belmokhtar et al. 2017, Belmokhtar et al. 2018, Zhang 2018, Liu et al. 2019, Zhang et al. 2019) and the key characteristics have been summarized by Armand et al. (2013, 2017a).

2.1. Short-term response

The main features of the short-term mechanical behaviour observed on claystone samples under triaxial compression, lateral decompression and extension tests can be summarized as follows: (a) linear elastic response under low deviatoric stress; (b) strain hardening from ∼50% of the peak strength; (c) strain softening for confining pressures lower than 20 MPa; (d) purely frictional residual behaviour governed by the induced shear bands and/or macro-cracks (Bésuelle and Lanata 2014; Hu et al. 2014, Menaceur et al. 2015, Desbois et al. 2017; Zhang 2016, Zhang et al. 2019). The post-peak behaviour is highly dependent on the confining pressure, characterized by a transition from brittle to ductile behaviour when the confinement exceeds the transition stress, σ_3^{bd}.

It has been shown that the classical Hoek and Brown (1980) failure criterion is suitable for describing both the elastic limit and peak shear strength of the COx claystone (Armand et al. 2013, 2017a, Souley et al. 2011, 2017, 2022, Zhang and Rothfuchs 2004, Zhang 2018). However, since the COx claystone in its natural state has no tectonic fractures, the classical meaning of the Hoek and Brown parameters cannot be used for interpreting the rock mass strength from laboratory tests. The residual strength can be approximated by a linear Mohr-Coulomb criterion for confinements below σ_3^{bd}, while Zhang and Rothfuchs (2004) or Zhang (2016) propose a Hoek-Brown envelope.

2.2. Volumetric contractance/dilatance mechanism

Experimental data of uni and triaxial compression tests typically exhibit a contractant behaviour (Chiarelli et al. 2003; Zhang and Rothfuchs 2004; Hoxha et al. 2007). At best, a dilatant response is sometimes observed near the residual strength under low confining pressures. Thus, the hypothesis of an associated flow rule usually overestimates the material dilatancy. Contractant or dilatant irreversible deformations are explained by two independent phenomena that occur during the post-peak phase (Conil et al. 2004). Herein, we will assume that there is a transition from volumetric compressibility to dilatancy at any given confinement and that this transition occurs earlier the lower confining stresses, in agreement with experimental data (Hu et al. 2014).

2.3. Damage mechanism

Triaxial tests with loading-unloading cycles do not indicate changes in elastic moduli before the peak strength (Armand et al. 2013, 2017a, Zhang and Rothfuchs 2004, Zhang et al. 2013, Zhang et al. 2019). Consequently, the proposed constitutive model does not consider the damage mechanism in the pre-peak phase. Instead, the observed non-linear stress-strain response is approximated by an elastoplastic mechanism with strain hardening. Conversely, biaxial, triaxial and radial extension tests (Bésuelle and Lanata 2014, Zhang 2016, Desbois et al. 2017, Zhang et al. 2019) clearly show the formation of shear bands and/or macro-cracks (individual or conjugate) in the post-peak phase (Zhang et al. 2019). These results are comparable to those obtained by other authors on the same rock (Hu et al. 2014, Menaceur et al. 2015, Belmokhtar et al. 2018).

Permeability measurements during triaxial compression tests have shown only small changes in the pre-peak stage and a drastic increase in the post-peak due to the occurrence of shear bands and macro cracks (Zhang and Rothfuchs 2004, Zhang 2016, Liu et al. 2018, Zhang et al. 2019). These observations agree with in situ permeability measurements in the CFZ around the MHM URL drifts (de la Vaissière et al. 2015).

To the authors' knowledge, there is no data about the strength, cohesion, or stiffness in the shear bands during the post-peak phase. Thus, isotropic damage is assumed here and modelled in the framework of CDM theory, considering a loss of strength and a reduction of stiffness.

2.4. Inherent anisotropy

Several experimental studies have been performed by several European laboratories to characterize the anisotropy of COx claystone in terms of static and dynamic modules and strengths (David et al. 2005, Sarout and Guéguen 2008, Zhang et al. 2012; Zhang et al. 2019, Zhang and Rothfuchs 2004, Menaceur et al. 2015, Mohajerani et al. 2012, Belmokhtar et al. 2017, 2018, Liu et al. 2019, Braun et al. 2021). These laboratory tests suggest an inherent anisotropy characterised by transverse isotropy and a slight anisotropy of the stiffness and strength. The Young's modulus is higher in the direction parallel to bedding than perpendicular to it with a ratio ranging between 1.2 and 2 (Zhang et al. 2012; Armand et al. 2013, 2017a, b; Zhang et al. 2019). Regarding the mechanical response, the transversely isotropic behaviour requires five independent constants, in general: Young's moduli parallel and perpendicular to the bedding (E_1, E_2), the shear modulus in the anisotropic plane G_{12} and Poisson's coefficients in the isotropic and anisotropic planes (ν_{13}, ν_{12}). The permeability is also anisotropic, with the corresponding ratio ranging between 2.5 and 10 (Zhang and Rothfuchs 2004). It should be noted that any induced fractures upon loading would add an "induced anisotropy" to the inherent anisotropy.

Experiments show similar strengths in the directions parallel and perpendicular to bedding. The lowest strength is observed at about 30°- 45° with respect to the bedding plane, depending on whether it consists of tensile or compressive strength. The ratio between minimum and maximum strength values is close to 0.7 for most of the performed tests (Zhang et al. 2019).

Andra has recently compiled experimental results of COx claystone peak strength as a function of the sample orientation with respect to the bedding plane (Figure 2a). The relative evolution of cohesion and tensile strength proposed by Manica et al. (2021) is illustrated in Figure 2b. Herein, we adopt this anisotropy for the elastic limit, the uniaxial compressive strength, and the residual cohesion.

2.5. Time-dependent behaviour

Several experimental studies of the long-term behaviour of the COx claystone have characterized the effect of confining pressure, mineralogical composition, or the degree of saturation on creep deformations (Gasc-Barbier et al. 2004, Fabre and Pellet 2006, Zhang et al. 2010, Armand et al. 2017a, Liu et al. 2018, Zhang et al. 2013, 2019, Zhang 2018), while in situ observations are summarized in (Armand et al. 2013, Armand et al. 2017a, b). The main features of the time-dependent response of the COx claystone can be summarized as follows (Armand et al. 2013, 2017a): (a) varying the loading rate in the range typically used in the laboratory has a small impact on the strength and is comparable with that resulting from mineralogical variability; (b) relaxation tests show a stabilization of the deviatoric stress a few days after loading; (c) volumetric strains during creep tests are negligible, as shown by simultaneous measurements of axial and lateral strains; (d) during secondary creep in some long-term tests, a non-linear increase in the creep strain rate with applied deviatoric stresses is observed. Fundamentally, creep strain rates slowly decrease with time, both for laboratory creep tests (Gasc-Barbier et al. 2004, Zhang et al. 2010, Zhang 2018) and in situ measurements of convergences and rock mass displacements around the M/HM URL drifts (Armand et al. 2013, Armand et al. 2017a, b).

A new campaign of creep tests under very low stresses and controlled hydric and thermal conditions is planned to further investigate the existence of a laboratory creep threshold. As mentioned in Section 1, in situ stress measurements at the MHM URL main level show a clear anisotropy (Wileveau et al. 2007). This suggests that if a relaxation of the initial deviatoric in situ stress occurred, then either it has not yet stabilized (which would indicate a very low deformation rate of the rock mass), or a deviatoric stress threshold below which creep is not activated should exist. Herein, despite this has not yet been experimentally demonstrated, we assume that there is a deviatoric stress threshold at which creep initiates. This threshold would be equal to the initial (in situ) deviatoric stress for modelling of MHM URL structures and zero for the laboratory tests (Souley et al. 2017, 2022).

Two families of models are mainly used to describe the creep behaviour of COx claystone: those using the Perzyna's overstress theory (Cuvilliez et al. 2017, Pardoen and Collin F 2017, Manica et al. 2021) and those based on an extension of the Lemaitre's model (Souley et al. 2011, 2017, Yu et al. 2021, Manica et al. 2017, Jung et al. 2022). Herein, we adopt the latter for which the parameters have been identified and referenced from numerous tests in Andra's database.

2.6. Hydromechanical coupling

The coupled hydromechanical behaviour of COx claystone has been thoroughly characterized with laboratory experiments based on various hydromechanical loading paths under saturated and unsaturated conditions (Chiarelli et al. 2003, Zhang and Rothfuchs 2004, Hoxha et al. 2007, Hu et al. 2014, Menaceur et al. 2015, Zhang et al. 2007, 2013, Belmokhtar et al. 2017, 2018).Published data shows significant scatter that may be related to the combination of different initial states of the cores and different experimental procedures (e.g. samples saturation or drainage system) adopted in the literature (Menaceur et al. 2015, Conil et al. 2018). Consequently, some values of poromechanical parameters are still under debate, such as the Biot coefficient. Escoffier (2002), Bemer et al. (2004), Belmokhtar et al. (2017) and Braun (2019) experimentally investigated the Biot coefficient of COx claystone under different confining pressures, and they obtained a range from 0.3 to 1 for this coefficient, with the mean value 0.6. However, recent research (e.g., Belmokhtar et al. 2017, Braun 2019) suggested a value of 0.8 for the Biot coefficient of COx claystone, which is currently being confirmed by further tests.

3. Proposed constitutive model

This section presents a phenomenological constitutive model of the transverse isotropic hydromechanical behaviour of COx claystone that simultaneously treats the different mechanisms discussed in Section 2. The choice of a phenomenological approach is motivated as some improvements can be easily incorporated to enrich the model according to new scientific advances.

3.1. Short-term behaviour

The short-term term behaviour of COx claystone is assumed linear elastic and transversely isotropic (requiring five parameters: E_1, E_2, G_{12}, ν_{13}, ν_{12}) below the elastic limit, followed by plastic strain hardening before the peak strength. The post-peak behaviour is modelled with damage mechanics coupled with plastic strain softening. This is followed by a residual perfectly plastic stage.

As previously discussed, the widely used Hoek-Brown (H-B) criterion (1980) has been applied to identify the elastic limit and peak strength of COx claystone based on numerous laboratory tests (Armand et al. 2013, 2017a, Zhang and Rothfuchs 2004, Zhang et al. 2019):

$$f_p(\sigma_3,\sigma_1) = -\sigma_1 + \sigma_3 - \sqrt{s\,\sigma_c^2 - \sigma_3\,m\,\sigma_c} = -\sigma_1 + \sigma_3 - \sqrt{B - \sigma_3\,A} \tag{1}$$

where σ_1 and σ_3 are the effective minor and major principal stresses (compressive stresses are negative, $\sigma_1 \leq \sigma_2 \leq \sigma_3$), m and s are the H-B material constants, σ_c is the stress corresponding to the elastic limit and peak stresses under unconfined compressive condition. A = m σ_c and B = s σ_c^2, are two independent parameters (Souley et al. 2011).

In our previous works, relation (1) was generalised in the space of three stress invariants (p, q, θ), where p is the effective mean stress, q the generalized deviatoric stress and θ the Lode's angle ($-30° \leq \theta \leq 30°$) (Souley et al. 2011, 2017, 2022). Here we adopt the generalised Mohr-Coulomb criterion in (p, q, θ) space but with the cohesion and friction angle (c, ϕ) derived from the Hoek-Brown parameters (m, s, σ_c) and the confining stress σ_3 in order to preserve the non-linear character of the elastic limit, peak and residual strengths of the COx claystone (eq. 1). More precisely and from a numerical point of view, the non-linear failure surface of H-B is continuously approximated by the M-C tangent at the current stress level, σ_3 (Hoek 1990, Lee and Bobet 2014). We recall the generalized form of Mohr-Coulomb criterion:

$$f_p(\boldsymbol{\sigma}) = q + p\, M_p - N_p$$
$$M_p = \frac{\sin\phi}{\left(\frac{\cos\theta}{\sqrt{3}} - \frac{1}{3}\sin\theta\sin\phi\right)} \quad ; \quad N_p = \frac{c\cos\phi}{\left(\frac{\cos\theta}{\sqrt{3}} - \frac{1}{3}\sin\theta\sin\phi\right)} \tag{2}$$

Where $\phi = \phi(\sigma_3)$ and $c = c(\sigma_3)$ (expressed in section 5.1) and p, q, θ have the following expressions:

$$p = \frac{\sigma_{ii}}{3}, \quad q = \sqrt{3J_2}\,, \quad \theta = \frac{1}{3}\sin^{-1}\left(\frac{-3\sqrt{3}}{2}\frac{J_3}{J_2^{3/2}}\right)$$
$$J_2 = \frac{1}{2}s_{ij}s_{ij}, \quad J_3 = \frac{1}{3}s_{ij}s_{jk}s_{ki}, \quad s_{ij} = \sigma_{ij} - p\delta_{ij} \tag{3}$$

Here J_2 and J_3 are the second and third invariants of the deviatoric stress tensor s_{ij}, respectively, and δ_{ij} is the Kronecker delta.

For confining stresses higher than σ_3^{bd}, the behavior of the COx remains ductile in consistency with the results of triaxial tests on samples (Armand et al. 2014, 2017) and is characterized by a residual strength identical to the peak strength (i.e., generalised Mohr-Coulomb deducted from Equation (1) with the Hoek-Brown parameters at the peak strength). Conversely, for confinements lower than σ_3^{bd}, the residual criterion is a straight line marked by a residual cohesion c_{res} and a residual friction angle ϕ_{res} determined as a function of the peak stress at σ_3^{bd} and c_{res}:

$$f_p(\boldsymbol{\sigma}) = q + p\,\frac{\sin\phi_{res}}{\left(\frac{\cos\theta}{\sqrt{3}} - \frac{1}{3}\sin\theta\sin\phi_{res}\right)} - \frac{c_{res}\cos\phi_{res}}{\left(\frac{\cos\theta}{\sqrt{3}} - \frac{1}{3}\sin\theta\sin\phi_{res}\right)} \quad (|\sigma_3| \leq \sigma_3^{bd}) \tag{4}$$

The residual behaviour remains perfectly plastic governed by the residual strength of the material (Hoek-Brown peak envelope or Mohr-Coulomb straight line depending on the value of σ_3 with respect to σ_3^{bd}). All this will be highlighted in section 5.2.2 (Verification of the short term behaviour).

For tensile stresses, we consider a «cut-off» of the mean effective stress to the value of tensile strength σ_t (in triaxial condition, i.e., B/A), leading to the following yield surface in tension:

$$f_t(\boldsymbol{\sigma}) = p - \sigma_t \tag{5}$$

In the pre-peak stage, the plastic hardening behaviour is represented by monotonic quadratic functions (C^2) of the two independent parameters A and B, between the elastic limit and the peak strength (Souley et al. 2017):

$$x = x_{ini} + \left\{x_{peak} - x_{ini}\right\}\left\{2 - \frac{\gamma_p}{\gamma_{p\_peak}}\right\}\frac{\gamma_p}{\gamma_{p\_peak}} \quad ; \quad x = \{A\,,B\} \tag{6}$$

where $A_{ini} = m_{ini}\sigma_{c\_ini}$ and $B_{ini} = s_{ini}\sigma_{c\_ini}^2$ are the parameters A and B at the elastic limit; $A_{peak} = m_{peak}\sigma_{c\_peak}$ and $B_{peak} = s_{peak}\sigma_{c\_peak}^2$ those at the peak, γ_p represents the internal plastic variable (i.e., plastic distortion or equivalent shear plastic strain) and γ_{p_peak} its corresponding value at the peak, and $\left(m_{ini}, s_{ini}, \sigma_{c\_ini}\right)$ and $\left(m_{peak}, s_{peak}, \sigma_{c\_peak}\right)$ are the H-B parameters (m, s, σ_c) at the elastic limit and peak strength, respectively. Thus, the pre-peak behaviour is governed by elasticity and plastic strain hardening without damage.

Regarding the post-peak phase between the peak strength and the residual stage, as evidenced by the results of laboratory characterisation, we will assume a transition between the strain softening and the ductile response depending on the confining pressure. In addition, the strain softening will be approached within the framework of isotropic Continuum Damage Mechanics (CDM). More precisely, the ductile behaviour (i.e., for confining stress $|\sigma_3| > \sigma_3^{bd}$) is modelled as perfectly plastic. On the contrary, the post peak stage for confining stress $|\sigma_3| < \sigma_3^{bd}$ is characterised by strain softening governed by a damage mechanism that results in a decrease in the effective moduli and a loss of strengths and cohesion by a factor of $(1 - d)$, where d represents the scalar damage variable. This damage is considered as isotropic and defined by the conjugate thermodynamic force (Y_d) based on the damage model of Mazars (1986) and similarly to Mohamad-Hussein and Shao (2007) or Chen et al. (2015):

$$f_d = d_{res}\left\{1 - \exp\left(-B_{d0}(Y_d - Y_{d0})\right)\right\} - d \leq 0 \tag{7}$$

where B_{d0} is the damage growth rate, Y_{d0} is the damage threshold related to Y_d at the peak strength, and d_{res} is the maximum damage reached at the beginning of the residual phase, which depends on the confining pressure or the effective mean stress.

The conjugate thermodynamic force associated with the damage variable is written using a pragmatic approach in which the damage evolution is related to the positive part of the total principal strains (i.e., extensional strain according to the stresses sign convention), as can be found in Mazars (1986).

$$Y_d = \sqrt{\langle \boldsymbol{\varepsilon} \rangle : \langle \boldsymbol{\varepsilon} \rangle} \tag{8}$$

where $\langle\ \rangle$ are the Macauley brackets: $\langle \varepsilon_i \rangle = 0$ if $\varepsilon_i < 0$ (compression) and $\langle \varepsilon_i \rangle = \varepsilon_i$ if $\varepsilon_i > 0$ (extension).

Large values of d_{res} are associated to low confining stresses and vice versa. However, we assume that under large confinements ($|\sigma_3| \geq \sigma_3^{bd}$), the material damage should be either absent or limited to diffuse damage. Consequently, beyond σ_3^{bd} there is no damage $(d = d_{res} = 0)$. More specifically, the brittle-ductile transition in the post-peak behaviour of COx claystone is introduced in the damage-induced strain softening, through the residual damage parameter d_{res}:

$$d_{res} = \begin{cases} 0 & ; \qquad \sigma_3 \leq -\sigma_3^{bd} \\ 1 - \eta_r & ; \qquad -\sigma_3^{bd} < \sigma_3 < 0 \end{cases} \tag{9}$$

Note that damage in presence of tensile stress $(0 < \sigma_3)$ is not considered in this research.

The influence of the confining pressure on the post-peak behaviour is then considered through the maximum residual damage, implemented by means of the ratio between the residual and the peak strengths η_r (also featuring the brittle-ductile transition):

$$\eta_r = \frac{(\sigma_1 - \sigma_3)_{res\_M-C}}{(\sigma_1 - \sigma_3)_{peak\_H-B}} \tag{10}$$

Note that η_r is defined with the extreme values of principal stresses σ_1 and σ_3, used in the classical H-B and M-C criteria. This choice is justified for reasons of simplicity and the lack of experimental data to quantify a possible dependence of η_r with the loading path (compression versus extension).

Equation (7) serves firstly as a criterion for crack propagation $(f_d > 0)$, but also for the evolution of the damage variable by solving $f_d = 0$, where the unknown is d. Knowing the damage threshold Y_{d0} allows damage to be initiated and propagated. The damage initiation (Y_{d0}) is computed internally the first time the peak strength is reached $(\gamma_p = \gamma_{p\_peak})$, then the corresponding value of Y_d in Equation 8 is assigned to Y_{d0}.

Finally, the damage affects the residual strength through a loss of cohesion, but also a degradation of the three elastic moduli. The residual cohesion c_{res} in Equation (4) is replaced by $(1 - d_{res})\ c_{res}$ while the elastic modules of the intact rock (undamaged) ${E_1}^0$, ${E_2}^0$ and ${G_{12}}^0$ are substituted by those of the damaged material $(1 - d){E_1}^0$, $(1 - d){E_2}^0$ and $(1 - d){G_{12}}^0$, respectively.

Based on the discussion in Section 2.2, a non-associated flow rule with the plastic potential proposed by Souley et al. (2022) is considered:

$$g(\boldsymbol{\sigma}, \gamma_p) = q + \beta(\gamma_p)\, p \tag{11}$$

with $\beta(\gamma_p)$ the dilatancy rate expressed as:

$$\beta(\gamma_p) = \begin{cases} \beta_m - (\beta_m - \beta_0) e^{-b_\beta \gamma_p} & ; \quad \gamma_p < \gamma_{ult} \\ \beta_{ult} exp\left(1 - \dfrac{\gamma_p}{\gamma_{ult}}\right) & ; \quad \gamma_p \geq \gamma_{ult} \end{cases} \tag{122}$$

The dilatancy rate evolves from an initial value β_0 to an asymptotic value β_m with the plastic distortion γ_p. b_β is the plastic flow velocity, γ_{ult} and β_{ult} represent the ultimate values of plastic deformation and dilatancy rate, respectively.

As discussed in Souley et al. (2022), it can be physically expected that the dilation will gradually vanish for large shear strains, reaching a purely frictional behaviour upon complete shearing of the fracture (or shear band) roughness. To account for this, a loss of dilation is assumed reflecting a shearing at constant volume. The ultimate plastic strain from which the dilatancy decreases is noted γ_{ult}. As indicated in Equation (12), beyond this plastic deformation, the dilatancy rate gradually decreases from the ultimate value $\beta_{ult} = \beta_m - (\beta_m - \beta_0) e^{-b_\beta \gamma_{ult}}$ to zero.

The uniaxial compressive stresses of the COx claystone (σ_c) at the elastic limit and peak strength, as well as the residual cohesion, are assumed to depend on the loading orientation with respect to the bedding planes (α), as suggested by experimental data (Section 2.4). Consequently, the variation of the instantaneous material cohesion and friction, $c(\sigma_3)$ and $\phi(\sigma_3)$, with the α is based on the concept of a tensor fabric (Pietruszczak et al. 2002), widely used to model the inherent and/or induced anisotropy. With this concept, directional material parameters are introduced into an anisotropic strength criterion based on microstructural observations. Strength anisotropy is therefore introduced using the microstructure tensor and by the strength parameters σ_{c_ini} at the elastic limit, σ_{c_peak} at the peak and the residual cohesion c_{res}:

$$\begin{aligned} \sigma_{c\_ini} &= \sigma_{c0\_ini}\left(1 + A_{ij} l_i l_j + a_1 (A_{ij} l_i l_j)^2 + a_2 (A_{ij} l_i l_j)^3\right) \\ \sigma_{c\_peak} &= \sigma_{c0\_peak}\left(1 + A_{ij} l_i l_j + a_1 (A_{ij} l_i l_j)^2 + a_2 (A_{ij} l_i l_j)^3\right) \\ c_{ani} &= c_{res}\left(1 + A_{ij} l_i l_j + a_1 (A_{ij} l_i l_j)^2 + a_2 (A_{ij} l_i l_j)^3\right) \end{aligned} \tag{13}$$

where σ_{c0_peak} and σ_{c0_ini} are the mean compressive strengths of the intact material; c_{res} is the mean residual cohesion; A_{ij}, a_1 and a_2 are the anisotropic parameters related to the material microstructure (Pietruszczak et al. 2002). In the absence of experimental data on the variation of yield stress at the elastic limit and residual strength with the angle α, only the microstructural parameters of the peak criterion are considered. Furthermore, the loading unit vector l_i is related to the generalized loading vector L_i defined from the stress tensor, $\widetilde{\boldsymbol{\sigma}}$ (expressed in the coordinate system of the bedding planes):

$$l_i = \frac{L_i}{\sqrt{L_k L_k}}, \quad L_i = L_j e_i^{(j)} = L_1 e_i^{(1)} + L_2 e_i^{(2)} + L_3 e_i^{(3)} \tag{14}$$

$$L_j = \sqrt{\tilde{\sigma}_{j1}{}^2 + \tilde{\sigma}_{j2}{}^2 + \tilde{\sigma}_{j3}{}^2}, \quad i, j = 1, 2, 3$$

where $e_i{}^{(k)}(k = 1, 2, 3)$ are the base vectors in the principal direction of the transverse isotropy. Since all quantities are expressed in the anisotropy reference system, l_3 is the component of the loading unit vector in the direction perpendicular to bedding. Consequently, if α is the angle between the normal vector to the bedding and the loading direction, then $cos\ \alpha = l_3$. In more general terms, if n_k and L_k represent respectively a vector normal to the bedding and the direction of loading (i.e., direction of the most compressive principal stress), the angle α is internally computed from the scalar product between these two vectors $\left(cos\ \alpha = {}^{n_k L_k}\!\big/_{\left(\sqrt{n_i n_i}\sqrt{L_j L_j}\right)}\right)$.

In Equation (13), the anisotropy parameter $A_{ij} l_i l_j$ is introduced to represent the projection of the microstructure tensor on the loading direction.

The microstructural tensor (A_{ij}) can be written as a function of their principal values (A_{11}, A_{22}, A_{33}) in the main axes. For the transverse isotropy of COx claystone, $A_{11} = A_{33}$ can be considered (Pietruszczak and Mroz 2000). In this case, the anisotropy of the initial plastic yield, peak strength and residual cohesion can be rewritten as:

$$\begin{aligned} \sigma_{c\_ini} &= \sigma_{c0\_ini}(1 + \lambda + a_1\lambda^2 + a_2\lambda^3) \\ \sigma_{c\_peak} &= \sigma_{c0\_peak}(1 + \lambda + a_1\lambda^2 + a_2\lambda^3) \\ c_{ani} &= c_{res}(1 + \lambda + a_1\lambda^2 + a_2\lambda^3) \\ \phi_{ani} &= \phi_{res}(1 + \lambda + a_1\lambda^2 + a_2\lambda^3) \end{aligned} \tag{15}$$

where $\lambda = A_{11}(1 - 3l_3^2)$. The parameters A_{11}, a_1, a_2, σ_{c0_peak}, σ_{c0_ini} and c_{res} can be calibrated in laboratory tests. In this paper, we adopt the same types of evolution of $\sigma_{c\_ini}/\sigma_{c0\_ini}$, $\sigma_{c\_peak}/\sigma_{c0\_peak}$ and c_{ani}/c_{res} with respect to the angle α as in Manica et al. (2021) (Figure 2b), i.e. the strengths at 0 are slightly lower than at 90° and the minimum strengths are reached at 45°.

Let us to recall the main assumptions: (a) the uniaxial compressive strength (at the elastic limit and the peak strength, σ_{c_ini} and σ_{c_peak}) depends on the orientation of the axial loading with respect to the bedding plane α, (b) the evolutions of σ_{c_ini} and σ_{c_peak} with respect to α are identical, and (c) for a general 3D stress tensor, α is determined by the orientation of the most compressive principal stress. The latter one represents a reasonably good approximation particularly in the range of compressive stresses. Subsequently, the general yield surfaces are expressed as a function of the full stress tensor and the angle α.

3.2. Long-term behaviour

The time-dependent behaviour of COx is governed by deformation processes corresponding to physical mechanisms at the microstructural level. Assuming the existence of a deviatoric stress threshold (Section 2) below which creep does not occur, a simplified form of the COx creep behaviour proposed in Souley et al (2017), an extension of the Lemaitre's model, is adopted here. The following equation was proposed for the viscoplastic strain tensor rate, $\dot{\boldsymbol{\varepsilon}}^{vp}$:

$$\dot{\boldsymbol{\varepsilon}}^{vp} = A_{visc} \langle \frac{q - q_0}{\sigma_0} \rangle^n {\varepsilon_{eq}}^{vp\,m} \frac{\partial q}{\partial \boldsymbol{\sigma}} \qquad (16)$$

where A_{visc} is the viscosity, q_0 the creep threshold, σ_0 the reference stress (typically one stress unit), n a dimensionless exponent corresponding to the deviatoric stress power factor, m the exponent of hardening work, $\boldsymbol{\sigma}$ the effective stress tensor, ${\varepsilon_{eq}}^{vp} = \sqrt{\frac{2}{3}\boldsymbol{\varepsilon}^{vp}:\boldsymbol{\varepsilon}^{vp}}$ the equivalent deviatoric creep strain, and $\boldsymbol{\varepsilon}^{vp}$ the creep strain tensor.

In Souley et al (2017), the material parameters A_{visc} and m change with the damage rate. As there is not sufficient data to establish such relationships, we refer either to the intact material with (A_0, m_0) or to the damaged material with the couple (A_1, m_1) and A_{visc} and m added in the model as a step function. More precisely, the parameters A_{visc} and m are therefore binary functions (a simple and pragmatic choice in first approximation), which can be improved in the future with new experimental data. From a numerical point of view, step functions are used to overcome numerical issues with linear variation when damage is between 0 and 0.1%:

$$A_{visc} = \begin{cases} A_0 & d = 0 \\ \alpha^A d + A_0 = \dfrac{A_1 - A_0}{10^{-3}} d + A_0 & 0 < d < 10^{-3} \\ A_1 & d \geq 10^{-3} \end{cases} \qquad (17)$$

$$m = \begin{cases} m_0 & d = 0 \\ \alpha^m d + m_0 = \dfrac{m_1 - m_0}{10^{-3}} d + m_0 & 0 < d < 10^{-3} \\ m_1 & d \geq 10^{-3} \end{cases} \qquad (18)$$

In section 6.4, we will revisit this consideration of the damage impact on creep strains by examining the absence of this influence (i.e., $\alpha^A = \alpha^m = 0$, $A_{visc} = A_0, m = m_0$).

For the purposes of simplicity, we do not consider here the anisotropy of the long term behaviour of the COx claystone as evidenced by recent experimental creep tests with several specimen orientations with respect to the bedding planes (Zhang et al. 2019). Nevertheless, as we are going to see in the model application, due to the anisotropy (in terms of the damage extent geometry and distribution of deviatoric stress) induced by the damage, the material exponent of hardening m and viscosity A_{visc} introduce a certain anisotropy of the viscoplastic strains and associated velocities.

3.3. Hydromechanical behaviour and induced permeability changes

In Comsol Multiphysics®, the coupling between fluid flow and deformation of porous media is described within the poromechanical framework (Coussy 2004; Detournay and Cheng 1993). This coupling is represented by (a) the Biot effective stresses concept (b) the effect of volumetric strain of the porous matrix on porosity, and (c) pore pressure change induced by the variation of fluid content.

The single-phase fluid flow in a porous medium is described by Darcy's law. The Darcy velocity, $\vec{v}_f$, is related to the pressure gradient according to:

$$\vec{v}_f = \frac{\boldsymbol{\kappa}}{\mu_f}\left(\vec{\nabla} p_f + \rho_f \vec{g}\right) \tag{19}$$

where $\boldsymbol{\kappa}$ is the permeability tensor, μ_f and ρ_f are respectively the fluid dynamic viscosity and density, p_f is the fluid pressure in the pores, $\vec{g}$ is the gravitational acceleration vector, and $\vec{\nabla}= \left\{\frac{\partial}{\partial x}, \frac{\partial}{\partial y}, \frac{\partial}{\partial z}\right\}$ is the gradient operator.

As discussed in Section 2.6, the Biot coefficient (α_B) and modulus (M) are both assumed isotropic herein. Then, the combination of Darcy's law and the continuity equation for conservation of fluid mass reads:

$$\rho_f \frac{1}{M}\frac{\partial p_f}{\partial t} + \vec{\nabla}.\rho_f\left[\frac{\boldsymbol{\kappa}}{\mu_f}\left(\vec{\nabla} p_f + \rho_f \vec{g}\right)\right] = Q_m - \rho_f \alpha_B \frac{\partial \varepsilon_{vol}}{\partial t} \tag{20}$$

with $\varepsilon_{vol} = tr(\boldsymbol{\varepsilon})$ is the volumetric strain, $\boldsymbol{\varepsilon}$ the strain tensor, $M = \frac{\varpi_p}{K_f} + \frac{(1-\alpha_B)(\alpha_B-\varpi_p)}{K_d}$, ϖ_p is the porosity, K_f the fluid bulk modulus, K_d the "equivalent" drained bulk modulus of the porous matrix, and Q_m a mass sink/source term.

Concerning the effect of damage on permeability, several constitutive models have been proposed in the literature and applied to laboratory tests and underground structures. These models mainly address the relationship between permeability variations and porosity, volumetric strain, damage variable (scalar or tensorial), plastic multiplier or deformation, or extensional deformations. Regarding the COx claystone, these are evolving with damage variable (Yu et al. 2021), with plastic deformation (Manica et al. 2017, 2021, Tourchi et al. 2021, Souley et al. 2017) or a combination between the induced limited shear plastic strain and the conceptual model of fracture zones around the MHM URL structures (Coarita-Tintaya et al. 2020, Souley et al. 2017). In the latter case and related to the conceptual model of EFZ (Armand et al. 2014), the empirical permeability model considers two domains. The first one is based on the CFZ concept, with a region of high and moderate increase in hydraulic properties due to the formation of macro fractures. The second one represents a region with micro-cracks, where changes in mechanical and hydraulic properties are not significant compared to e.g., uncertainty in measurements.

Permeability changes have been measured around MHM URL structures as a function of both the direction and the distance from the drift walls (Armand et al. 2014). In laboratory tests, permeability increases when the percolation threshold is reached (Zhang et al. 2019). Despite this experimental evidence, it is at present cumbersome to relate these variations to mechanical quantities. In this paper, we propose a simple phenomenological formulation based on 2 internal variables that may be potential candidates for the evolution of hydraulic properties in the EFZ:

$$\boldsymbol{\kappa} = \boldsymbol{\kappa_0}\, f({d_{rat}}^*) g({\gamma_{SF}}^*) \tag{21}$$

where $\boldsymbol{\kappa_0}$ and $\boldsymbol{\kappa}$ are the permeability tensors of the intact material and damaged (cracking and shear failure) material. The internal variables are: (a) the damage rate, ${d_{rat}}^* = \frac{d}{d_{res}}$, representing the value of the current damage divided by the maximum damage reached at the beginning of the residual phase d_{res}. It is the degree of damage where zero value is associated to the intact rock and unity to the damaged material and, (b) a so-called fracturing rate, ${\gamma_{SF}}^* = \frac{\gamma_p}{\gamma_{ult}}$, related to shear failure.

Finally, f and g are two independent scalar functions to be fitted from laboratory measurements and in situ observations. For simplicity, linear forms are adopted here: $f(x) = 1 + \alpha_{dam}\, x$ and $g(y) = 1 + \alpha_{SF}\, y$, with x and y two variables between 0 and 1, α_{dam} and α_{SF} two model constants.

4. Model regularisation

Selection of a given technique depends among other factors on the calculation code used. For example, the non-local integral method can be found e.g., in Cast3M (Giry et al. 2011) or Plaxis (Rezania et al. 2012, Manica et al. 2018). In Comsol Multiphysics®, regularisation with the implicit gradient method is relatively easy to implement and shows good numerical stability and has thus been adopted in this work. The implicit gradient technique (Peerlings et al. 1996b) is a robust class of non-local methods (Geers et al. 2000), which computes a non-local average of a local equivalent variable, considering the non-local value as an additional degree of freedom governed by the solution of the Helmholtz differential equation (Zreid and Kaliske 2018). Models based on implicit gradients show good computational efficiency and numerical stability (Simone 2007, Schreter et al. 2018).

In the proposed model, two internal variables are regularised: the damage variable and the equivalent shear plastic strain. The regularisation scheme is based on the non-local implicit gradient (e.g., non-local average $\tilde{\xi}_{eq}$ of the corresponding local internal variable ξ_{eq} is computed by considering the non-local value as an additional degree of freedom governed by the solution of the Helmholtz differential equation also known as free energy potential):

$$\tilde{\xi}_{eq} - {l_\xi}^2\, \nabla^2 \tilde{\xi}_{eq} = \xi_{eq} \tag{22}$$

where l_ξ is the characteristic length associated to the internal local variable ξ_{eq}, representing the length scale that determines the influence radius of the interaction.

First, we regularised the damage variable using this equation with the local thermodynamic force that drives damage (Y_d): in other words, $\tilde{\xi}_{eq} = \tilde{Y}_d$, $\xi_{eq} = Y_d$ and $l_\xi = l_d$. Then the variable Y_d is replaced in Equation (7) of the damage evolution. Note that the value of Y_{d0} parameter is also determined with respect to the regularised variable.

With regards to the internal shear plastic strain variable, which also needs to be regularised, thanks to recent developments in Comsol Multiphysics® since the version 6.0, the plastic distortion (or even porosity) can be regularised with the implicit gradient (eq. 22) for all elastoplastic models (already available in Comsol or Used Defined Models). This Comsol built-in implementation of regularisation scheme was therefore used, requiring only the introduction of the characteristic length $l_\xi = l_{\gamma_p}$.

The characteristic lengths l_d and l_{γ_p} are material parameters that specify the size of the regions over which the local variables are averaged. By considering a larger characteristic length than the distance between adjacent evaluation nodes (defined by mesh size and element order), mesh-size independency can be ensured. Conversely, values of characteristic length close to 0 should correspond to the classical local approaches (without regularisation schemes), i.e., numerical solutions dependent on the spatial discretization.

The characteristic length is usually related to material heterogeneities (Bazant and Pijaudier-Cabot 1989, Geers et al. 1998, Le Bellego et al. 2003). For concrete, the characteristic length has been postulated to be proportional to the diameter of the largest aggregates (Bazant and Pijaudier-Cabot, 1989). For COx, there is no well accepted criterion to define it. The values of l_d and l_{γ_p} adopted in this study are of the same order of magnitude as those used for the characteristic length in other existing advanced models of COx claystone at drift scale (Yu et al. 2021, Manica et al. 2021). In addition, a sensitivity analysis on this parameter was carried out and is presented in Section 6.5. Nonetheless, it is recognised that a smaller value should be used if localization of damage at laboratory scale (i.e., cm-scale) was simulated.

5. Numerical implementation and verification

5.1. Implementation method in Comsol Multiphysics®

For the numerical implementation and in order to overcome and to overcome the possible negative values of the term under the square root of the non-linear Hoek-Brown (H-B) criterion (eq. 1), we adopt a simplified approach using an equivalence between the H-B and the Mohr-Coulomb (M-C) criteria for each confining stress σ_3 (Figure 3). In fact, the non-linear failure surface of H-B is continuously approximated by the M-C tangent at the current stress level, σ_3 (Hoek 1990, Lee and Bobet 2014). This approximation remains true because the entire mechanical model is built on the assumption of small transformations, which means that terms of order greater than 2 are neglected. Such an approach is implemented in e.g., *FLAC^{3D}* code and makes it possible to easily perform the safety factor computations using the non-linear H-B failure criterion.

The current tangent M-C criterion depending on both the instantaneous angle of friction $\phi(\sigma_3)$ and cohesion $c(\sigma_3)$ can be expressed as follows:

$$\sigma_1 = \sigma_3\, N_{\phi(\sigma_3)} - 2\, c(\sigma_3)\sqrt{N_{\phi(\sigma_3)}} \quad ; \quad N_{\phi(\sigma_3)} = \frac{1 + \sin\phi(\sigma_3)}{1 - \sin\phi(\sigma_3)} \tag{23}$$

where $\phi(\sigma_3)$ and $c(\sigma_3)$ are derived from the current slope of the H-B envelope:

$$\phi(\sigma_3) = 2\tan^{-1}\sqrt{N_{\phi(\sigma_3)}} - \frac{\pi}{2}; \qquad c(\sigma_3) = \frac{\sigma_c^{ucs}}{2\sqrt{N_{\phi(\sigma_3)}}} \tag{24}$$

with

$$N_{\phi(\sigma_3)} = 1 + \frac{A}{2}(B - A\,\sigma_3)^{-\frac{1}{2}}; \quad \sigma_c^{ucs} = \sigma_3\big(N_\phi - 1\big) + (B - A\,\sigma_3)^{\frac{1}{2}} \tag{25}$$

Thus, for a given stress level σ_3, expressions (24) and (25) can be used to determine the local M-C criterion with Equation (23). Finally, this local criterion in (σ_1, σ_3) plane can be rewritten in the space of stress invariants (p, q, θ) according to equation (2) as function of $c(\sigma_3)$ and $\phi(\sigma_3)$.

Finally, the proposed constitutive model is implemented into Comsol Multiphysics® v6.0 using three modules. The Solid Mechanics module solves for the anisotropic elastoplastic, damage and viscoplastic model, the Domain ODEs and DAEs are used for storing history variables, and the Helmholtz Equation module is used for the regularisation (Figure 4). These modules are written in strong form and solved based on finite element method (weak form). A similar implementation strategy was followed by Zhou et al. (2018) for a phase-field model.

The algorithm to solve for the anisotropic elastoplastic and damage model is summarized below.

1) Previous value of computed damage (d^{k-1}) and current total strain ($\boldsymbol{\varepsilon}^k$) are used to calculate current effective stress tensor ($\boldsymbol{\sigma}^k$).
2) Elastoplastic anisotropic yield function: $f_{p,t}\big(\boldsymbol{\sigma}^k, \gamma^{p^k}, d^{k-1}\big) = 0$ is solved to find current plastic strains ($\boldsymbol{\varepsilon}^{p^k}$).
3) Current damage (d^k) is calculated based on the total strain, to be used in the next time step ($k + 1$).

As previously mentioned since version 6.0 of Comsol Multiphysics®, a regularisation of the equivalent plastic strain is available for elastoplastic models through the implicit gradient method with the Helmholtz equation (22). Therefore, we will use the regularisations of the local variables Y_d, Y_{d0} and γ_p, in the forthcoming applications of the proposed model.

5.2. Verification of the numerical implementation

5.2.1. Input parameters

All the parameters used are summarized in Table 1. The most common ones used in rock mechanics result from laboratory characterizations carried out on COx claystone samples during the last two decades and is currently part of Andra's database. Some of the published references of these data can be found in Su (2003), Chiarelli et al. (2003), Armand et al. (2013), Armand et al. (2017b), Seyedi et al. (2017), Zhang et al. (2010, 2012, 2019), etc. The transverse isotropic characteristics (moduli and permeabilities) have been more recently characterized. The values considered correspond to the average values reported by Armand et al. (2013). The Poisson's ratios represent the values recently used by Manica et al. (2021), Tourchi et al. (2021) and Yu et al. (2021). As mentioned previously, an isotropic Biot coefficient with an average value of 0.6 is adopted (Armand et al. 2017, Seyedi et al. 2017).

Numerous experimental data indicate that a failure criterion based on the parabolic criterion of Hoek and Brown (1980) is suitable for describing the shear strength of the Callovo-Oxfordian claystone (Su 2003, Armand et al. 2013, 2017, Zhang 2016, 2018; Zhang and Rothfuchs 2004). The fitting leads to the identification of two sets of parameters m, s and $\sigma_c$for the elastic limit and peak strength: an “average” one obtained by best fit of Hoek and Brown criterion from experimental data and a “lower” one which represents the lower bound of these data. As discussed in Souley al. (2022), the “lower” values are most suitable to represent the COx claystone relative to the in situ observations: this is also assumed in this paper. An initial average residual cohesion c_{res} of 0.8 MPa is assumed, being reduced by a factor of $(1-d_{res})$ with the damage mechanism during the softening stage. The parameters related to plastic flow were adopted from Souley et al. (2022) since they were suitable to reproduce the laboratory tests. The growth rate of the damage B_{d0} is taken equal to 150, while the residual friction ϕ_{res} and damage threshold Y_{d0} are internally computed: the first at the initialization and the second once the peak strength is reached.

Finally, regarding the anisotropy of the yield stress σ_c at the elastic limit (σ_{c_ini}) and peak (σ_{c_peak}), and the residual cohesion (c_{ani}) as a function of angle α, the parameters A_{11}, a_1 and a_2 were calibrated according to the dimensionless curve shown in Figure 2b ($A_{11}=0.2$, $a_1=2$ and $a_2=-1.5$). In other words, these anisotropic parameters of tensor fabric correspond to a minimum strength at 45°, while the strength at 0° is slightly lower than that at 90° with a ratio of 1.25 (Manica et al. 2021, Djouadi et al. 2020).

For the time-dependent behaviour, parameters are those identified from the first series of creep tests (Su 2003) and represent the creep parameters of intact COx claystone. They will be used to simulate a more recent series of creep tests (Armand et al. 2017), thus not used in their identification in contrast to the values proposed in Souley et al. (2017). The creep parameters related to the damaged material are the most difficult to obtain as there is a lack of data on the time-dependent behaviour of the damaged COx claystone, despite an attempt to perform creep tests at 75 and 90% of the COx peak strength (Armand et al. 2017). Then, values of A_1 (viscosity) and m_1 (strain hardening exponent) were identified by trial-and-error calibration on the measured convergences around the GCS: the retained values are 1.88 x 10^{-25} $1/_s$ and -4.25, respectively.

Similarly for the evolution of permeability as a function of damage and shear fracture, the following values 50 and 2.75 were used for α_{dam} and α_{SF}, respectively. They could be more precisely determined if experimental data in the post-peak regime were available.

5.2.2. Short term response

The first verification of the proposed model and its numerical implementation aims to demonstrate the ability of the model to reproduce the brittle-ductile transition of the material for a transition confining stress (σ_3^{bd}) of 25 MPa. Triaxial compression tests with different confining pressures (-0.001, -1, -2, -5, -10, -20, and -30 MPa) are simulated. Figure 5a presents the corresponding deviatoric stress - axial strain curves for different confining pressures. The post-peak behaviour is confining pressure dependent and the transition stress between brittle failure and ductile behaviour is clearly marked. The resulting curves display four stages (elastic, hardening in pre-peak, softening in post-peak and residual phases) when the confining pressure is below the transition stress level σ_3^{bd}, but only three stages (elastic, hardening and perfect plastic phase) under high confining pressure. Figure 5b compares the values of the elastic limit, the peak and the residual strengths for different confining stress with the theoretical envelopes. A good agreement can be observed between numerical results and analytical solutions since the relative error for peak strength is less than 0.1%, and 3% for the elastic limit and the residual strength, respectively. The reason why the residual envelope is not a straight line with slope ϕ_{res} for $|\sigma_3| < |\sigma_3^{bd}|$ is explained by the cohesion decrease with the damage at the beginning of the residual regime, d_{res}. Recall that the latter is maximum in the absence of confinement and null at σ_3^{bd}.

The second verification of the instantaneous response using the proposed model focuses on the simulation of a triaxial test with different axial loading directions with respect to the bedding, α: 0° (perpendicular to bedding), 30°, 45°, 60° and 90° (parallel to bedding), for a confinement of -2 MPa. Figure 6a presents the corresponding deviatoric stress - axial strain curves for different orientation, while Figure 6b shows comparison between the simulated and theoretical plasticity threshold, peak, and residual strengths. In particular, the model predicts the orientation dependence of strength, which corresponds well with the theoretical initial, peak, and residual anisotropic strengths.

5.2.3. Long term response

To investigate the model response for the time-dependent behaviour of COx, triaxial compression creep tests of 90 days duration at different deviatoric stresses (50%, 75% and 90% of the peak strength estimated to be 36.5 MPa, i.e., 18.25; 27.375 and 32.85 MPa) reported by Armand et al. (2017), were selected for numerical prediction. Figure 7a compares the model and the theoretical (eq. 16) results of the time evolution of the deviatoric creep strain. A very good agreement is observed (maximum deviation below 0.1%). Figure 7b compares the evolution of the axial creep strain as a function of time between our simulations and the laboratory tests. Then, the model with the COx creep parameters from the Andra database allows to adequately reproduce these tests, despite they were not used to identify the input parameters. Finally, differences between modelled and experimental strains are similar to those obtained by several authors (Cuvilliez et al. 2017, Manica et al. 2017, Pardoen and Collin 2017, Souley et al. 2017, Coarita-Tintaya et al. 2020, Yu et al. 2021), whose input parameters of their model were calibrated on these 3 creep tests. This suggests that the deviation is of the same order of magnitude as the heterogeneity of this rock.

6. Application to GCS drift

6.1. Why the choice of GCS drift?

As mentioned in the introduction, the GCS drift remains a challenge for numerical modelling, since to our knowledge, very few authors (Manica et al. 2021 and Yu et al. 2021) have successfully proposed a constitutive model of COx claystone behaviour with an appropriate regularisation scheme able to properly reproduce most of the in situ observations. Specifically, they are the anisotropies of the EFZ extension, of the convergences, of the pore pressure distribution, etc., while the initial stress state in the GCS drift section is quasi-isotropic (sv = 12.7 MPa, sh = 12.4 MPa). It is also a very interesting case that allows to validate the constitutive models, their numerical implementation and possibly to help in the back-calibration of certain model parameters. For all these reasons, we have chosen this gallery for an operational hydromechanical application of the model proposed with Comsol Multiphysics® software.

6.2. Hydromechanical model

We refer to the benchmarking specifications carried out by several teams for the numerical modelling of GCS drift (parallel to sH) and since then taken up in subsequent publications (Manica et al. 2021, Yu et al. 2021). The assumptions and specifications for the hydromechanical modelling under saturated conditions are given next and are detailed in Seyedi et al. (2017). A circular gallery is considered with a radius of 2.6 m and assuming 2D plane strain configuration. Rock bolts and the support system are not explicitly modelled. The initial stress (total) state is the one prevailing at the main level (-490 m) of the URL and discussed in the introduction, with an initial pore pressure of 4.7 MPa. The excavation is simulated by decreasing the total radial stress to the mean value of 0.3 MPa (a deconfining rate of 98% equivalent to a shotcrete/rock bolts support) for a period of 28 days (corresponding to an average advance speed of 0.357 m/day). Hydraulically, the GCS wall is subjected to a constant water pressure of 4.7 MPa during the first 13 days and zero after 15 days, with a linear variation between 13 and 15 days. The geometrical model and the initial and boundary conditions are shown in Figure 8a, while Figure 8b displays the adopted finite element mesh. In the annulus bounded by the radii 2.6 m (gallery wall) and 7.8 m, there are 40 elements in the radial direction and 60 elements in the orthoradial direction (mesh M40x60Q), according to geometric and arithmetic progressions, respectively. In this annulus, finer mesh is used in the zone close to the GCS wall. Figure 8c shows the average extension of EFZ from the in situ observations (Figure 1) as well as the location of pore pressure measurements along the horizontal borehole OHZ1521 used for comparison with the numerical simulations.

First, the reference case with the mesh M40x60Q will be discussed, considering the impact of damage on both permeability and creep strains as well as that of shear failure on permeability. Numerical results will be compared with in situ observations and measurements in terms of EFZ extension and time evolution of convergences and pore pressure in PR02, PR03, PR04 and PR05 chambers. In a second step, these dependencies on viscous strains and permeability will be gradually removed, in order to evaluate their influences. Finally, the independence of the results on the mesh size will be examined and discussed in the Appendix. The reference mesh (Figure 8b) is characterized in particular by quadrangular elements in the annular around the GCS drift.

6.3. Results and discussion

6.3.1. Extent of damage and plastic zones: comparison with the observed EFZ extent

The extension of the damaged zones (expressed in terms of the ratio between the damage variable and the maximum damage reached at the beginning of the residual phase, $d_{rat}{}^{*}$) from the end of excavation (28 days) up to 4 years, is shown in Figure 9a. The iso-values of the plastic shear strain accumulated during the pre-peak and residual phases are drawn in Figure 9b. It can be noted that after 2 months (one month after the excavation end), the extensions of damaged and plastic zones reach almost steady state. Most of the damage and plastic strain are concentrated around the wall of GCS drift. It can be seen that the damage next to the lateral walls of the drift shows no localization but rather a continuous pattern. Moderate band-pattern distribution can be found at the outer region, the width of these bands being related to the characteristic length (0.08 m). These continuous-like results are similar to Yu et al. (2021), who used a regularisation scheme of their finite element solution based on the phase field. On the contrary, Pardoen and Collin (2017) and Manica et al. (2021) obtained rather localized discrete bands of shear plastic strain in this region. Manica et al. (2021) regularised their rheological model by a non-local integral formulation in the finite element code PLAXIS while Pardoen and Collin (2017) used the local second gradient in the finite element code LAGAMINE. A pattern with more localized discrete bands would have been obtained for a different ratio between characteristic length and mesh size (see Appendix).

In the following, the predicted extents of damaged or shear failed zones (post-peak and/or residual phases) will be referred to by DZ, while the plastic shear zones in the pre-peak phase are designated by ZSF. Table 2 summarises the various zones of fractures around the GCS drift, both observed and numerically predicted. For structures of MHM URL oriented in the direction of the principal major horizontal stress, the average and maximum values of the CFZ and DFZ extensions observed are also given in this table.

Comparison of the damaged and plastic zones predicted by models based on continuous approaches with the in situ observations of discrete and/or connected explicit fractures zones around underground structures in semi-brittle rocks is cumbersome. Nevertheless, these damaged and/or plastic zones in continuous approaches can be regarded or interpreted as homogenized (or upscaled) fracture zones. Thus, as adopted in Souley et al. (2022), the zone closest to the drift wall, where the excavation induces softening and residual regimes (DZ extent in the proposed model), can be considered as the observed CFZ. In turn, the zone where only hardening regime occurs during the excavation (ZSF extent in the proposed model), is associated to the DFZ. By drawing this analogy between model and in situ observations (Armand et al. 2014), a good agreement can be observed, as shown in Figure 10. The DZ extent obtained with the model agrees well with in situ observations. The average and maximum of CFZ extent observed at the main level of MHM URL for drifts oriented parallel to σ_H, are 0.2xD and 0.4xD at the drift sides (respectively, 0.1xD and 0.15xD at the roof), D being the diameter of the drift (Figure 10a). Conversely, the numerical simulation underestimates the extension of ZSF compared to the observed DFZ. As discussed in Section 6.3.3, this will have a significant impact on the evolution of the pore pressure around the interface between DFZ and intact rock.

6.3.2. Convergences around the GCS drift

Figure 11 compares the modelled and in situ measured evolution of horizontal and vertical convergences of the GCS drift wall. The strong anisotropic response (which is related to the EFZ shape) observed in situ is well reproduced by the model. The measured anisotropic convergence has a ratio C_h/C_v ~1.5-2.1, whereas the model results in ratios of 1.3-1.9. The latter value is reached at the beginning of the stabilisation of the DZ extent associated with a post-peak behaviour (60 days). The predicted evolution of the horizontal and vertical convergences, as well as their magnitudes are in quite good agreement with in situ measurements. This has only been reproduced by few rheological models with a post-peak phase and requiring a regularisation method (Pardoen and Collin 2017, Manica et al. 2021 and Yu et al. 2021) or introducing the anisotropy of viscosity into the predefined EFZ (Jung et al. 2022).

6.3.3. Pore pressure in borehole OHZ1521 and other horizontal boreholes

Figure 12 compares the modelled and the in situ measured pore pressure evolution at 4 points of the horizontal profile (OHZ 1521). These points correspond to chambers located at distances of 1.1; 1.9; 4.8 and 9.9 m from the GCS wall, i.e., distances of: 0.2xD, 0.4xD, 0.9xD and 1.9xD. In relation to the observed and predicted EFZ, the first two points are located inside the CFZ and DZ zones, respectively. Inversely, the third point (PRE_04) would be inside the DFZ zone, whereas numerically it is predicted to be in the intact matrix at about one radius from the ZSF. The simulation allows to reproduce the pore pressure peak in the chambers located close to the GCS wall (PRE02 and PRE03): 6.2 MPa against the 6.6 MPa observed in situ. It also reproduces the pore pressure drops after the forehead passage. On the other hand, the model does not reproduce the measured overpressure in chamber PRE04. In reality, this zone is possibly subject to elastic contraction during the passage of the front, which would reduce the porosity and therefore the intrinsic permeability, thus increasing the Skempton effect (interstitial suppression). Furthermore, the modelled extent of the DFZ remains underestimated compared to the in situ observations, leading to an underestimation of the damage-induced permeability increase and thus the pressure drop highlighted by Vu et al. (2020) or Manica et al. (2021).

Figure 13 illustrates the evolution of the modelled (at 200 days, 1, 2, 3 and 4 years) and in situ measured pore pressures around the GCS drift as a function of time. This figure clearly indicates a zone of drainage (with almost zero pore pressure) or hydraulically disturbed zone in the horizontal direction of the GCS drift. This zone is of one diameter extension, coinciding with the EFZ extent observed in situ. Conversely, numerically this drainage zone would be limited to the DZ domain, i.e., the average extension of the observed CFZ. Thus, to be able to reproduce this observed hydraulically disturbed zone from the pressure measurements (Figure 13), it would be necessary to further calibrate the evolution of the permeability both in the DZ and in the EFZ, while also calibrating the extension of the latter (decrease of the elastic limit for example).

Finally, the proposed model allows to reproduce qualitatively and quantitatively most of the pore pressure measurements conducted in situ around the GCS drift.

6.3.4. Radial displacements (extensometer) in the rock mass along the horizontal borehole OHZ1501

The radial displacement inside the rock mass has been followed by the installation of borehole extensometers, in which mine-by-test experiment is installed before the excavation of the GCS drift from other existing drift (borehole OHZ1501 in Figure 1c). In this section, only the radial displacements in the first chambers (DFO_01 to 05) of the horizontal borehole OHZ1501 are analyzed. These points inside the COx are located at distances of 0.2; 0.8; 1.8; 3.3 and 4.8 m (i.e., 0.04xD, 0.15xD, 0.35xD, 0.6xD and 0.9xD, respectively) from the wall of the GCS. Those of the additional 5 chambers (DFO_06 to 10) located between 5.8 and 24.8 m from the GCS wall measured virtually zero displacements and have not been represented for clarity.

Figure 14 displays measured and predicted relative radial displacement between the head of the extensometer (wall) and points inside the COx for horizontal borehole (OHZ1501). Except for the near-wall point (DFO_01), where the radial displacement is well correlated with the horizontal convergence, the radial displacements for the 3 points DFO_02, DFO_03 and DFO_04 appear to be underestimated by the model. As these points are all located within the zone of connected fractures (based on the maximum extension of CFZ), we can therefore be questioned about the influence of the behaviour of these fractures (their openings in particular) on their displacements, which cannot be correctly reproduced assuming a continuous model. On the other hand, the relative displacement of the point located in the intact rock (DFO_05) is better reproduced by the model compared to the three previous ones and to the results of Jung et al. (2022).

Even if the magnitude of the measured displacements is not properly reproduced with the model, it can be noted that the predicted radial displacement velocities along borehole OHZ1501 remain consistent with the observations.

6.4. Effect of damage and fractures on the viscoplastic strain and permeability changes

In order to evaluate the sensitivity of taking into account the impact of damage and shear failure on the results, 3 additional calculations were performed. Case 1 stems from the reference case but without considering the coupling between permeability and the rates ${d_{rat}}^*$ and ${\gamma_{SF}}^*$. Case 2 restates the reference case by deactivating the influence of damage on the creep deformations ($m_1 = m_0$; $A_1 = A_0$) but maintaining a variable permeability tensor. Finally, Case 3 is a combination of cases 1 and 2, i.e. no coupling between damage and shear failure on the creep strains and on the permeability tensor is considered. The reference case (Ref) is the one studied in the previous section and integrates the effects of damage and shear failure on the viscoplastic deformations and the permeability tensor. This section allows also to check the consistency between the input parameters values and the numerical results, and a first impact of the individual input parameters.

Figure 15 highlights the impact of shear yield and damage on the permeability and viscous strains. As in the reference case, the extension of the plastic and damaged zones reaches steady state one month after the end of excavation. Still, the magnitudes of the damage variable and the plastic strain increase with time in these zones. The impact of permeability (constant versus variable) is clearly illustrated by comparing the reference case with Case 1 and, Case 2 with Case 3. In both instances, the constant permeability (therefore of lower amplitude) tends to accentuate the undrained response inside the rock mass in the direction of the minor stress (σ_h), which is also associated with the lower modulus of deformation (anisotropy of elastic moduli). In other words, more interstitial overpressures are then dissipated in the near field, leading to larger damage and plastic strains. This is clearly illustrated in Figure 16, representing the pressure profile in the horizontal direction at 4 different times. It also shows the reduction of the drainage rate when the permeability is kept constant and equal to that of the intact matrix.

The effect of damage and shear failure on viscoplastic strains and permeability changes, is also examined through the evolution in time of GCS convergences (Figure 17). In relation to the extensions of damaged and shear failed zones discussed below, it can be noted that, when comparing the reference scenario to Case 1, the increase in the extent of the damaged zones one month after excavation is accompanied by an increase in convergence, despite the decrease in displacements induced by drainage (less important in Case 2): here the predominant mechanism is damage-induced creep. The similarity between the two simulations on the vertical convergence is explained by the fact that the roof is not damaged, and the plastic strains remain low, thus leading to limited permeability variations. Finally, Figure 18 illustrates the results of the sensitivity analysis on the deformation within the rock. The same trends are found as for the convergences.

In conclusion, this sensitivity analysis demonstrates the complex interplay between damage, creep and diffusion of the fluid mass. In particular, with a constant permeability (equal to that of the intact rock), considering the creep of the damaged rock increases the displacements (Case 1 versus Case 3). Conversely, by not considering the creep of the damaged or sheared rock (Case 2 versus Case 3), the use of a variable permeability field (damaged and/or plastic rock being more permeable than intact ones) reduces the magnitude of displacements despite a more important drainage, which is less intuitive. Therefore, the couplings between damage, creep, and transport properties on the one hand, but also between creep and permeability changes on the other hand, need to be investigated in further depth. Finally, for the overpressure and under-pressure inside the rock mass respectively in the directions parallel and perpendicular to the bedding, it could be interesting to investigate the impact of the instantaneous elastic volumetric deformation (thus variation of porosity) on the field of initial permeability (i.e., induced changes of permeability due to the elastic volumetric strain).

6.5. Sensitivity analysis on characteristic length: effect on the volumetric and plastic shear strains, damage, and permeability changes

In this section we examine the influence of characteristic length on the distribution of volumetric strain, plastic shear strain, permeability in the bedding plane and damage rate. The reference case (used in all the simulations discussed previously) consists of the mesh shown in Figure 8b and two identical characteristic lengths $l_{\gamma_p} = l_d = 8\ \mathrm{cm}$. In this sensitivity analysis, we also consider identical characteristic lengths, l_c for the local damage and plastic strain variables. Lower and higher values than the reference value, are studied: 2, 6, 10, 15 cm (i.e., from ¼ to 2 times the reference value).

In Figure 19 we summarised the distribution of the considered variables along the horizontal profile (where the highest variations are expected in relation to the induced damage) for the last time of simulation (t=1500 d). For sake of reading, we have limited ourselves to 1.2xD from the GCS wall (variations beyond this distance are negligible). For each of the four quantities represented in this figure, three distinct domains can be distinguished: one corresponding to the quasi-continuous damaged zone adjacent to the GCS wall, the second associated with strain hardening (plasticity) and elasticity, and the third representing a transition zone between the two previous ones. In the first two, the distribution of damage and/or plastic distortion is continuous, leading to a monotonic evolution of these variables. The transition zone is instead associated with localised bands of damage and plastic strain already illustrated in Figure 9, which lead to a series of jumps in the studied variables. It is precisely in this transition zone that the influence of l_c on the results remains most marked.

Independently to the value of l_c, the variation in volume (Figure 19a) remains governed by the damage mechanism, with dilatant volumetric strain in the first domain. Moreover, in this domain, the volumetric plastic deformation is also dilatant, but 2.5 to 5 times lower than the total volumetric strain. In the second domain (plastic), the volumetric behaviour is still globally contractant (even if it is dilating after an initial elastic contraction).

The evolution of permeability (Figure 19c) is also highly correlated with the distribution of damage (Figure 19d).

In conclusion, despite the damage scattering associated to localised bands in the transition zone, the results remain globally independent to the value of characteristic length in the investigated range (between ¼ and twice the reference value)).

7. Conclusion

In France, the National Radioactive Waste Management Agency (Andra) oversees the study of a disposal for intermediate-level long-lived (IL-LLW) and high-level activity radioactive waste (HLW) in a deep claystone formation (Callovo-Oxfordian claystone, COx) in the framework of the Cigéo project. Several in situ and laboratory THM characterization studies have been undertaken in this formation since 2000. In parallel, theoretical analyses, constitutive models and numerical modelling have been developed to describe different processes during the life of the disposal.

The present paper is a part of ongoing collaborative scientific research on the development of advanced constitutive models for COx claystone behaviour and robust numerical tools suitable for the THMC modelling (1D, 2D and 3D) in the Cigéo project and available in an industrial software. Based on available experimental data, an anisotropic elastoplastic, damage and viscoplastic model is then proposed to describe the mechanical behaviour of the COx claystone. The model considers state-of-the-art knowledge of the THM behaviour of COx claystone and focuses on the key mechanisms. Among these mechanisms, we can mention: the nonlinear instantaneous and delayed mechanical responses, the anisotropy of the THM behaviour as well as the anisotropy of strengths. As for most semi-brittle geomaterials, the mechanical behaviour of COx claystone is marked by a strain softening mechanism, after the peak strength. Consequently, appropriate modelling of these geomaterials behaviour requires the use of a regularisation technique to overcome the problem of mesh dependence and hence to better represent the development of the EFZ (Excavation-induced Fractured Zones) particularly around the structures of MHM-URL. The proposed model was implemented with a regularisation scheme based on the non-local implicit gradient for two internal variables (damage viewed in the framework of Continuum Damage Mechanics and equivalent shear plastic strain) in the commercial finite element code, Comsol Multiphysics®, which allows multiple physics to be simultaneously considered.

After validating the implemented model on simple stress paths (triaxial compression and creep tests), its operational nature is successfully evidenced on the GCS drift (// σ_H) for which the in situ observations and measurements are the most challenging to reproduce (Manica et al. 2021). Specifically, by drawing an analogy between the numerical damaged zone and the observed connected fracture zone (CFZ), a good agreement is obtained between observations and the numerical simulation. The model allows to reproduce the pore pressure peak in sensors near the GCS wall as well as the pore pressure drop after the forehead passing. The convergences are also well reproduced as well as their ratios (horizontal/vertical). Typically, the observed ratios ranged between 1.3 and 2.1 while those predicted are comprised between 1.3 and 1.9.

The perspective will be to incorporate the creep strain anisotropy, the temperature-dependent creep strain, as well as an extension to hydromechanical coupling under unsaturated conditions.

8. References

Aifantis EC (1984) On the microstructural origin of certain inelastic models. J Eng Mater Technol 106(4):326–330

Armand G, Dewonck S, J-M, Bosgiraud, Richard-Panot L (2015) Development and new research program in the Meuse Haute Marne Underground Research Laboratory (France). 13th ISRM International Congress of Rock Mechanics

Armand G, N Conil, Talandier J, Seyedi DM (2017a) Fundamental aspects of the hydromechanical behaviour of Callovo-Oxfordian claystone: from experimental studies to model calibration and validation. Computers and Geotechnics 85:277-286

Armand G, Noiret A, Zghondi J, Seyedi DM (2013) Short- and long term behaviors of drifts in the Callovo-Oxfordian claystone at the Meuse/Haute-Marne Underground Research Laboratory. J Rock Mech Geotech Eng 5(3):221–230

Armand G, Bumbieler F, Conil N, de La Vaissière, Bosgiraud JM, Vu MN (2017b), Main outcomes from in situ THM experiments programme to demonstrate feasibility of radioactive HL-ILW disposal in the Callovo-Oxfordian claystone, J Rock Mech Geotech Eng, 9(3), 415-427

Armand G, Leveau F, Nussbaum C, de La Vaissiere R, Noiret A, Jaeggi D, Landrein P, Righini C (2014) Geometry and properties of the excavation induced fractures at the Meuse/Haute-Marne URL drifts. Rock Mech Rock Eng 47(1):21–41. doi:10.1007/s00603-012-0339-6

Askes H, Sluys LJ (2002) Explicit and implicit gradient series in damage mechanics, European Journal of Mechanics - A/Solids, 21 (3), 379-390, https://doi.org/10.1016/S0997-7538(02)01214-7

Bazant ZP, Belytschko TB, Chang TP (1984) Continuum theory for strain softening. J Eng Mech 110(12):1666–1692

Bažant ZP, Jirásek M (2002) Nonlocal integral formulation for plasticity and damage: survey of progress, Journal of Engineering Mechanics, ASCE, 128, 1119-1149

Bazant Z P, Pijaudier-Cabot G (1989) Measurement of Characteristic Length of Nonlocal Continuum. J Eng Mech 115(4):755–767

Belmokhtar M, Delage P, Ghabezloo S, Menaceur H, Tang AM, Conil N (2017) Poroelasticity of the Callovo–Oxfordian claystone. Rock Mech Rock Eng 50:871–889. https://doi.org/10.1007/s0060 3-016-1137-3

Belmokhtar M, Delage P, Ghabezloo S, Conil N (2018) Drained Triaxial Tests in Low-Permeability Shales: Application to the CallovoOxfordian Claystone. Rock Mechanics and Rock Engineering, Springer Vienna, 51(7), 1979–1993

Bemer E., Longuemare P., Vincké O. (2004) Poroelastic parameters of Meuse/Haute-Marne argillites: effect of loading and saturation states. Applied Clay Science 26, p. 359-366

Bésuelle P, Lanata P (2014) Characterization of the early strain localization in a sandstone and a clay rock. Cambridge, UK, 1-3 September 2014

Bian H, Zhang X, Shao JF (2017) A coupled elastoplastic and visco-plastic damage model for hard clay and its application for the underground gallery excavation, Underground Space, 2, 60-72

Braun P (2019) Thermo-hydro-mechanical behavior of the Callovo-Oxfordian claystone: Effects of stress paths and temperature changes. PhD thesis, Paris-Est University

Braun P, Ghabezloo S, Delage P, Sulem J, Conil N (2021) Thermo-Poro-Elastic Behaviour of a Transversely Isotropic Shale: Thermal Expansion and Pressurization. Rock Mechanics and Rock Engineering (2021) 54:359–375 https://doi.org/10.1007/s00603-020-02269-y

Chen L, Wang CP, Liu JF, Liu J, Wang J, Shao, JF (2015) Damage and Plastic Deformation Modeling of Beishan Granite Under Compressive Stress Conditions. Rock Mech Rock Eng, 48, 1623–1633. https://doi.org/10.1007/s00603-014-0650-5

Chiarelli AS, Shao JF, Hoteit N (2003) Modeling of elastoplastic damage behavior of a claystone, *International Journal of Plasticity*, 19, 23-45

Coarita-Tintaya ED, Golfier F, Souley M, Vu MN (2020) Anisotropic hydro-viscoplastic modelling of a drift at the Meuse/Haute-Marne URL. European Journal of Environmental and Civil Engineering. DOI: 10.1080/19648189.2020.1797887

Conil N, Djeran-Maigre I, Cabrillac R, Su K (2004) Poroplastic damage model for claystones*, Applied Clay Science*, 26, 473-487

Conil N, Talandier J, Djizanne H, de La Vaissière R, Righini-Waz C, Auvray C, Morlot C, Armand G (2018) How rock samples can be representative of in situ condition: A case study of Callovo-Oxfordian claystones. Journal of Rock Mechanics and Geotechnical Engineering 10(4):613–623

Coussy O (2004) Poromechanics. John Wiley & Sons, Ltd, 2004. — XVI + 298 p. — ISBN: 0-470-84920-7

Cosserat E, Cosserat F (1909) Théorie des Corps Déformables. Hermann, Paris

Chambon R, Caillerie D, Matsushima T (2001) Plastic continuum with microstructure, local second gradient theories for geomaterials: localization studies. Int J Solids Struct, 38(46- 47):8503–8527

Cuvilliez S, Djouadi I, Raude S, Fernandes R (2017) An elastoviscoplastic constitutive model for geomaterials: Application to hydromechanical modelling of claystone response to drift excavation, *Computers and Geotechnics*, 85, 321-340

David C, Robion P, Menendez B (2005) Anisotropy of elastic, magnetic and microstructural properties of the Callovo-Oxfordian shales (Meuse). in: 2nd Int Meeting Clays in Natural & Engineered Barriers for Radioactive Waste Confinement

Djouadi I, Giot R, Raude S, Cuvilliez S, Laigle F, Fernandes R (2020) Integration of Transverse Isotropy in the Instantaneous Behaviour of Geomaterials with Application to Numerical Modelling of Underground Structures. Geotech Geol Eng (2020) 38:4917–4938. https://doi.org/10.1007/s10706-020-01336-z

de Borst R, Mühlhaus HB (1992) Gradient-dependent plasticity: formulation and algorithm aspects. Int J Numer Meth Eng 35(3):521–539

de Borst, R., Sluys, L. J., Mühlhaus, H-B., Pamin, J. (1993) Fundamental issues in finite element analyses of localization of deformation, *Engng Comput*, 10, 99-121

de Borst, R., and Sluys, L.J. (1991) Localisation in a Cosserat continuum under static and dynamic loading conditions, Computer Methods in Applied Mechanics and Engineering, 90, 805-827

de la Vaissière R, Armand G, Talandier J (2015) Gas and water flow in an excavation-induced fracture network around an underground drift : A case study for a radioactive waste repository in clay rock. Journal of Hydrology 521:141-156

de Saint-Venant B. (1863) Sur la distribution des élasticités autour de chaque point d'un solide ou d'un milieu de contexture quelconque, particulièrement lorsqu'il est amorphe sans être isotrope. J de Mathématiques Pures et Appliquées, Série 2, Vol. 8, pp. 353-430 ; 257-295

Detournay E, Cheng AHD (1993) Fundamentals of poroelasticity. In C. Fairhurst (Ed.), Comprehensive rock engineering: Principles, practice and projects. Vol. II. Analysis and design method (pp. 113–171). Pergamon Press

Desbois G, Höhne N, Urai JL, Bésuelle B, Viggiani G (2017) Deformation in cemented mudrock (Callovo–Oxfordian Clay) by microcracking, granular flow and phyllosilicate plasticity: insights from triaxial deformation, broad ion beam polishing and scanning electron microscopy. Solid Earth, 8, 291–305, 2017

Desrues J, Viggiani G (2004) Strain localization in sand: an overview of the experimental results obtained in Grenoble using stereophotogrammetry. Int. J. Numer. Anal. Meth. Geomech., 28, 279-321. https://doi.org/10.1002/nag.338

Dinç Göğüş Ö, Scholtès L (2018) Discrete Analysis of Damage and Shear Banding in Argillaceous Rocks. Rock Mechanics and Rock Engineering. 51. 10.1007/s00603-017-1397-6.

Escofer S (2002) Caractérisation expérimentale du comportement hydroméchanique des argilites de Meuse/Haute-Marne. PhD thesis, Institut National Polytechnique de Lorraine

Fabre G, Pellet F (2006) Creep and time-dependent damage in argillaceous rocks. Int J Rock Mech Min Sci 2006;43:950–60

Gasc-Barbier M, Chanchole S, Bérest P (2004) Creep behavior of Bure clayey rock. Applied Clay Science. 26(1–4), August 2004, 449-458. https://www.sciencedirect.com/science/article/abs/pii/S016913170300293X

Geers MGD, de Borst R, Brekelmans WAM, Peerlings RHJ (1998) Strain-based transient-gradient damage model for failure analyses. Comput Methods Appl Mech Eng 160:133–53. https://doi.org/10.1016/S0045-7825(98)80011-X

Geers MGD, Peerlings RHJ, Brekelmans WAM (2000) Phenomenological nonlocal approaches based on implicit gradient-enhanced damage, Acta Mechanica 144, 1–15, https://doi.org/10.1007/BF01181824

Giry C, Dufour F, Mazars J (2011) Stress-based nonlocal damage model, International Journal of Solids and Structures, 48, 3431-3443

Hoek E, Brown ET (1980) Empirical strength criterion for rock masses, Journal of the Geotechnical Engineering Division, ASCE 106(GT9), 1013-1035

Hoek E (1990) Estimating Mohr-Coulomb friction and cohesion values from the Hoek-Brown failure criterion, Int J Rock Mech Min Sci & Geomech Abst, 27, 227-229

Hoxha D, Giraud A, Homand F, Auvray C (2007) Saturated and unsaturated behavior modelling of Meuse/Haute-Marne argillite. *Int J Plast*, 23, 733–66

Hu DW, Zhang F, Shao JF (2014) Experimental study of poromechanical behavior of saturated claystone under triaxial compression. Acta Geotechnica, 9(2), 207–214

Jia Y, Bian HB, Su K, Kondo D, Shao JF (2009) Elastoplastic damage modeling of desaturation and resaturation in argillites, *Int. J. Numer. Anal. Meth. Geomech*., 34, 187–220

Jirásek M (2007) Nonlocal damage mechanics, Revue Européenne de Génie Civil, 11:7-8, 993-1021, doi: 10.1080/17747120.2007.9692974

Jung S, Vu MN, Pouya A, Ghabezloo S (2022) Effect of anisotropic creep on the convergence of deep drifts in Callovo-Oxfordian claystone. Computers and Geotechnics

Le Bellego C, Dube JF, Pijaudier-Cabot G, Gerard B (2003) Calibration of non local damage model from size effect tests. European J Mech A/Solids, 22, 33-46

Lee Y, Bobet A (2014) Instantaneous Friction Angle and Cohesion of 2-D and 3-D Hoek–Brown Rock Failure Criteria in Terms of Stress Invariants. *Rock Mech Rock Eng*, 47, 371-385

Lekhnitskii SG (1981) Theory of Elasticity of an Anisotropic Body. Moscow: Mir Publishers

Lemaitre J (1985) A Course on Damage Mechanics, second ed. Springer

Liu ZB, Xie SY, Shao JF, Conil N (2018) Multi-step triaxial compressive creep behaviour and induced gas permeability change of clay-rich rock Géotechnique 68:281–289 https://doi.org/10.1680/ jgeot.16.P.117

Liu, Z., Shao, J., Xie, S., Conil, N., Talandier, J. (2019) Mechanical Behavior of Claystone in Lateral Decompression Test and Thermal Effect. Rock Mechanics and Rock Engineering, Springer Vienna, 52(2), 321–334

Lu X, Bardet J-P, Huang M (2009) Numerical solutions of strain localization with nonlocal softening plasticity. Comput. Methods Appl. Mech. Engng. 198 (47–48), 3702–3711

Mánica MA, Gens A, Vaunat J, Armand G, Vu MN (2022) Numerical simulation of underground excavations in an indurated clay using non-local regularisation. Part 1: Formulation and base case. Geotechnique, 72(12):1092–112

Mánica MA, Gens A, Vaunat J, Ruiz D-F (2018) Nonlocal plasticity modelling of strain localisation in stiff clays, Computers and Geotechnics, 103, 138-150

Mánica MA, Gens A, Vaunat J, Ruiz D-F (2017) A time-dependent anisotropic model for argillaceous rocks. Application to an underground excavation in Callovo-Oxfordian claystone. Computers and Geotechnics, 85:341–350

Mazars J (1986) A description of micro- and macroscale damage of concrete structures. Engineering Fracture Mechanics, 25(5-6), 729-737

Menaceur H, Delage P, Tang AM, Conil N (2015) The thermomechanical behaviour of the Callovo-Oxfordian claystone. International Journal of Rock Mechanics and Mining Sciences, 78, 290–303

Miehe C, Aldakheel F, Mauthe S (2013) Mixed variational principles and robust finite element implementations of gradient plasticity at small strains. Int J Numer Methods Engrg. 94 (11), 1037–1074

Mohajerani M, Delage P, Sulem J, Monfared M, Tang AM, Gatmiri B (2012) A laboratory investigation of thermally induced pore pressures in the Callovo-Oxfordian claystone. Int J Rock Mech Min Sci 52:112–121

Mohamad-Hussein A, Shao JF (2007) An elastoplastic damage model for semi-brittle rocks, Geomechanics and Geoengineering, 2:4, 253-267, DOI: 10.1080/17486020701618329

Mühlhaus H-B (1989) Application of Cosserat theory in numerical solutions of limit load problems, Ing. Arch., 59, 124-137

Pardoen B, Levasseur S, Collin F (2015) Using Local Second Gradient Model and Shear Strain Localisation to Model the Excavation Damaged Zone in Unsaturated Claystone. Rock Mech Rock Eng, 48(2):691–714. doi: 10.1007/s00603-014-0580-2

Pardoen B, Collin F (2017) Modelling the influence of strain localisation and viscosity on the behaviour of underground drifts drilled in claystone. Computers and Geotechnics 85 (2017) 351–367

Patzák B, Jirásek M (2004) Adaptive Resolution of Localized Damage in Quasi-brittle Materials. *Journal of Engineering Mechanics*, 130, 720–732

Peerlings RHJ, de Borst R, Brekelmans WAM, de Vree JHP (1996b) Gradient-enhanced damage for quasi-brittle materials. Int J Numer Meth Eng 39:3391–3403

Peerlings RHJ, de Borst R, Brekelmans WAM, de Vree JHP, Spee I (1996a) Some observations on localisation in non-local and gradient damage models. Eur J Mech A/Solids 15(6):937–953

Perzyna P (1966) Fundamental problems in viscoplasticity. Adv Appl Mech 1966;9

Pijaudier-Cabot G, Bazant ZP (1987) Nonlocal damage theory. J Eng Mech 113(10):1512–1533

Pietruszczak S, Mroz Z (1981) Finite element analysis of deformation of strain-softening materials, Int J Mum Meth Engng, 17, 327-334

Pietruszczak S, Mroz Z (2000) Formulation of anisotropic failure criteria incorporating a microstructure tensor, Computers and Geotechnics, 26, 105-112

Pietruszczak S, Lydzba D, Shao JF (2002) Modelling of inherent anisotropy in sedimentary rocks, Int. J. Solids Struct., 39, 637-648

Read HE, Hegemier GA (1984) Strain softening of rock, soil and concrete — a review article, *Mechanics of Materials*, 3, 271-294

Rezania M, Bonnier P, Brinkgreve R, Karstunen M (2012) Non-local regularisation of Drucker-Prager softening model, Proceedings of the 20th UK Conference of the Association for Computational Mechanics in Engineering 27 – 28th March 2012, the University of Manchester, Manchester

Sabet SA, de Borst R (2019) Structural softening, mesh dependence, and regularisation in non-associated plastic flow, *Int J Numer Anal Methods Geomech*, 43, 2170– 2183

Sarout J, Guéguen Y (2008) Anisotropy of elastic wave velocities in deformed shales. Part I: Experimental results. Geophysics 73/5, D75-D89

Schreter M, Neuner M, Hofstetter (2018) Evaluation of the implicit gradient-enhanced regularization of a damage-plasticity rock model, Appl Sci-Basel 8 (6)

Seyedi DM, G Armand, Noiret A (2017) Transverse Action – A model benchmark exercise for numerical analysis of the Callovo-Oxfordian claystone hydromechanical response to excavation operations. Computers and Geotechnics 85, 287-305

Simone A (2007) Explicit and implicit gradient-enhanced damage models, Revue Européenne de Génie Civil, 11:7-8, 1023-1044, doi: 10.1080/17747120.2007.9692975

Souley M, Vu MN, Armand G (2022) 3D Modelling of Excavation-Induced Anisotropic Responses of Deep Drifts at the Meuse/Haute-Marne URL. *Rock Mech Rock Eng*, 55, pages 4183–4207 (2022) https://doi.org/10.1007/s00603-022-02841-8

Souley M, Armand G, Kazmierczak J-B (2017) Hydro-elasto-viscoplastic modeling of a drift at the Meuse/Haute-Marne underground research laboratoratory (URL). Computers and Geotechnics 85 (2017) 306–320

Souley M, Armand G, Su K, Ghoreychi M. (2011) Modelling of the viscoplastic behaviour including damage for deep argillaceous rocks. Physics and Chemistry of the Earth 2011;36:1949–59

Stefanou I, Sulem J, Rattez H (2017) Cosserat approach to localization in geomaterials. In: Handbook of nonlocal continuum mechanics for materials and structures. Springer

Sulem J (2010) Bifurcation theory and localization phenomena. European Journal of Environmental and Civil Engineering, Taylor & Francis, 14, 989-1009

Summersgill FC, Kontoe S, Potts DM (2017) Critical Assessment of Nonlocal Strain-Softening Methods in Biaxial Compression, Int. J. Geomech., 17, 04017006

Tourchi S, Vaunat J, Gens A, Bumbieler F, Vu MN, Armand G (2021) A full-scale in situ heating test in Callovo-Oxfordian claystone: observations, analysis and interpretation. Computers and Geotechnics 133, 104045. doi.org/10.1016/j.compgeo.2021.104045

Trivellato E, Pouya A, Vu MN, Seyedi D (2019) A softening damage-based model for the failure zone around deep tunnels in quasi-brittle claystone. In Proceedings "Tunnels and Underground Cities: Engineering and Innovation meet Archaeology", WTC 2019 ITA-AITES World Tunnel Congress, Naples, Italy, pp. 4242–4251. doi:10.1201/9780429424441-449

Tsang CF, Bernier F, Davies C (2005) Geohydromechanical processes in the excavation damaged zone in crystalline rock, rock salt, and indurated and plastic clays—in the context of radioactive waste disposal. Int J Rock Mech Min Sci 42(1):109–125

Valanis KC, Peters JF (1996) Ill-posedness of the initial and boundary value problems in non-associative plasticity, *Acta Mech*., 114, 1-25

Vu MN, Guayacán-Carrillo L-M, Armand G (2020) Excavation induced over pore pressure around drifts in the Callovo-Oxfordian claystone. European Journal of Environmental and Civil Engineering. doi.org/10.1080/19648189.2020.1784800

Wu S, Wang X (2010) Mesh dependence and nonlocal regularization of one-dimensional strain softening plasticity. J Eng Mech 136(11):1354–1365

Wileveau Y, Cornet FH, Desroches J, Blumling P (2007) Complete in situ stress determination in an argillite sedimentary formation. Physics and Chemistry of the Earth, 32(8-14):866–878

Yanqiu H, Shao JF (2013) A micromechanical analysis of time-dependent behavior based on subcritical damage in claystones. Int J Damage Mech 2013;22:773–90

Yao C, Shao JF, Jiang QH, Zhou CB (2017) Numerical study of excavation induced fractures using an extended rigid block spring method. Computers and Geotechnics 85:368-383

Yu Z, Shao JF, Duveau G, Vu MN, Armand G (2021) Numerical modeling of deformation and damage around underground excavation by phase-field method with hydromechanical coupling. Computers and Geotechnics 138, 104369. doi.org/10.1016/j.compgeo.2021.10436

Zhang C-L, Armand G, Conil N, Laurich B (2019) Investigation on anisotropy of mechanical properties of Callovo-Oxfordian claystone. Engineering Geology 251 (2019) 128–145

Zhang C-L. (2016) The stress-strain-permeability behaviour of clay rock during damage and recompaction. J Rock Mech. and Geotech. Engng 8(2016) 16-26

Zhang C-L (2018) Thermo-hydro-mechanical behavior of clay rock for deep geological disposal of high-level radioactive waste. Journal of Rock Mechanics and Geotechnical Engineering, Elsevier Ltd, 10(5), 992–1008

Zhang C, Rothfuchs T (2004) Experimental study of the hydromechanical behaviour of the Callovo-Oxfordian argillite. Applied Clay Science, Elsevier, 26(1–4), 325–336

Zhang F, Jia Y, Bian HB, Duveau G (2013) Modeling the influence of water content on the mechanical behavior of Callovo–Oxfordian argillite. Physics and Chemistry of the Earth 65 (2013) 79–89

Zhang F, Xie SY, Hu DW, Shao JF, Gatmiri B (2012) Effect of water content and structural anisotropy on mechanical property of claystone. Appl Clay Sci 69:79–86

Zhang CL, Czaikowski O, Rothfuchs T (2010) Thermo-hydro-mechanical behavior of the Callovo-Oxfordian clay rock, GRS-266. Germany: GRS; 2010

Zhou S, Rabczuk T, Zhuang X (2018) Phase field modeling of quasi-static and dynamic crack propagation: COMSOL implementation and case studies, Advances in Engineering Software, 122, 31–49

Zhou S, Zhuang X, Rabczuk T (2019) Phase field modeling of brittle compressive-shear fractures in rock-like materials: A new driving force and a hybrid formulation, Computer Methods in Applied Mechanics and Engineering, 355, 729-752

Zreid I, Kaliske M (2018) A gradient enhanced plasticity–damage microplane model for concrete. Comput Mech 62, 1239–1257. https://doi.org/10.1007/s00466-018-1561-1

9. Appendix

Illustration of mesh-independency on the results of GCS drift simulation

This section is dedicated to the evaluation of the effect of the mesh size on the numerical results presented in this paper in terms of extensions of damaged and plastic zones, drift convergences, pore pressure distribution and deformation of the rock mass in the near and far fields. For this, we started from the last configuration discussed above (Case 3). The reference mesh is the one used in all the simulations previously discussed, i.e., M40x60Q consisting of 40 x 60 quadrilateral elements in an annulus of one GCS diameter from the wall (i.e., 40 radial elements with a geometric progression, 60 orthoradial elements with an arithmetic distribution). Coarser and finer meshes were used, especially around the GCS drift wall. They are summarized in Table A1.

For these different meshes, the extension of the damaged and plastic zones, the pressure along the horizontal profile for different times, the evolution of the GCS convergences and the displacement in the massif are shown in Figures A1 to A4. They indicate a quasi-absence of mesh dependence, which was not the case when no regularisation scheme was used (Coarita-Tintaya et al. 2020). However, moderate differences are obtained in terms of 2D distribution of the damaged zone. For the cases in which the selected characteristic length (0.08 m) is close to the distance between evaluation nodes, an almost continuous pattern is found. In turn, for the most spatially refined case, the large ratio between characteristic length and mesh size results in a more localized discrete band pattern in which its width is defined by the characteristic length selected.

Table 1 - List of input parameters and the used values.

Parameter	Value	Unit	Description
${E_1}^0$	8000	MPa	Young's modulus in the plane of isotropy ($E_\parallel$) for undamaged rock
${E_2}^0$	4000	MPa	Young's modulus normal to the isotropy plane ($E_\perp$) for undamaged rock
ν_{12}	0.35		Poisson coefficient normal to the isotropy plane ($\nu_{\parallel\perp}$)
ν_{13}	0.24		Poisson coefficient in the isotropy plane ($\nu_{\parallel\parallel}$)
${G_{12}}^0$	1806.5$^{(1)}$	MPa	Shear modulus normal to the isotropy plane ($G_{\parallel\perp}$) for undamaged rock
m_{ini}	1.5		Hoek-Brown parameter at the elastic limit
m_{peak}	2		Hoek-Brown parameter at the peak strength
s_{ini}	1		Hoek-Brown parameter at the elastic limit
s_{peak}	0.128		Hoek-Brown parameter at the peak strength
σ_{c0_ini}	9.6	MPa	Elastic limit stress under unconfined compressive condition
σ_{c0_peak}	33.5	MPa	Peak stress under unconfined compressive condition
c_{res}	0.8	MPa	Residual cohesion
σ_3^{bd}	25	MPa	Transitional stress between brittle – ductile behaviour
γ_{peak}	0.00225		Peak plastic distortion
γ_{ult}	0.01125		Ultimate plastic distortion
β_0	-0.1		Initial compressibility/dilatancy rate
β_m	0.3		Asymptotic compressibility/dilatancy rate
b_β	600		Plastic flow velocity
B_{d0}	150		Damage growth velocity
A_{11}	0.119$^{(2)}$		Anisotropic parameter related to the microstructure tensor
a_1	10.442$^{(2)}$		Anisotropic parameter
a_2	6.195$^{(2)}$		Anisotropic parameter
A_0	8×10^{-25}	1/s	Viscosity at room temperature of the intact (undamaged) rock
n	6.8		Exponent of the deviatoric stress
m_0	-2.7		Exponent for hardening work of the undamaged material
ϖ_p	0.18		Porosity
α_B	0.6		Equivalent isotropic Biot coefficient
$k_{//}$	4×10^{-20}	m^2	Intrinsic permeability in the plane of isotropy
$k_\perp$	1.333×10^{-20}	m^2	Intrinsic permeability in any plane normal to the isotropy plane
$l_{\gamma_p} = l_d$	0.08	m	Characteristic lengths for model regularisation

(1) In absence of experimental data, G_{12} can be expressed as a function of the 4 other elastic constants through the empirical relation proposed by Lekhnitskii (1981) which is a particular case of de St Venant (1863).

(2) fitted parameters based on the U-shape of the peak strength measured on COx samples (Figure 2a).

Table 2 - Abbreviations of different zones around the GCS drift.

Abbreviations	Description
EFZ	Excavation-induced Fractures Zone (observation or numerical)
CFZ	Connected Fractured Zone, refer to the conceptual model of fracturation observed around the M/HM URL excavations (Armand et al. 2014)
DFZ	Discrete Fractured Zone, refer also to the conceptual model of fracturation (Armand et al. 2014)
DZ	Damaged Zone, refer to the numerically predicted extents of damaged or shear failed zones (post-peak and/or residual phases)
ZSF	Zone of Shear Failure, refer to the numerically predicted extents of shear failed zones during the pre-peak regime (or hardening phase)

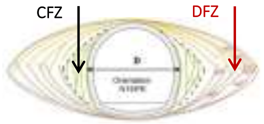

Conceptual model of **EFZ** for drifts parallel to σ_H (Armand et al. 2014)

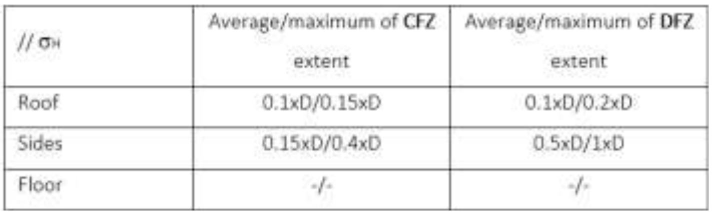

// σ_H	Average/maximum of **CFZ** extent	Average/maximum of **DFZ** extent
Roof	0.1xD/0.15xD	0.1xD/0.2xD
Sides	0.15xD/0.4xD	0.5xD/1xD
Floor	-/-	-/-

Table A1 - Sensitivity analysis on mesh size.

In graph legends	Name	Number of radial elements	Number of orthoradial elements
Mesh-3	M11x16Q	11	16
Mesh-2	M13x20Q	13	20
Mesh-1	M25x40Q	25	40
Ref	M40x60Q	40	69
Mesh+1	M56x80Q	56	80
Mesh+2	M84x120Q	84	120

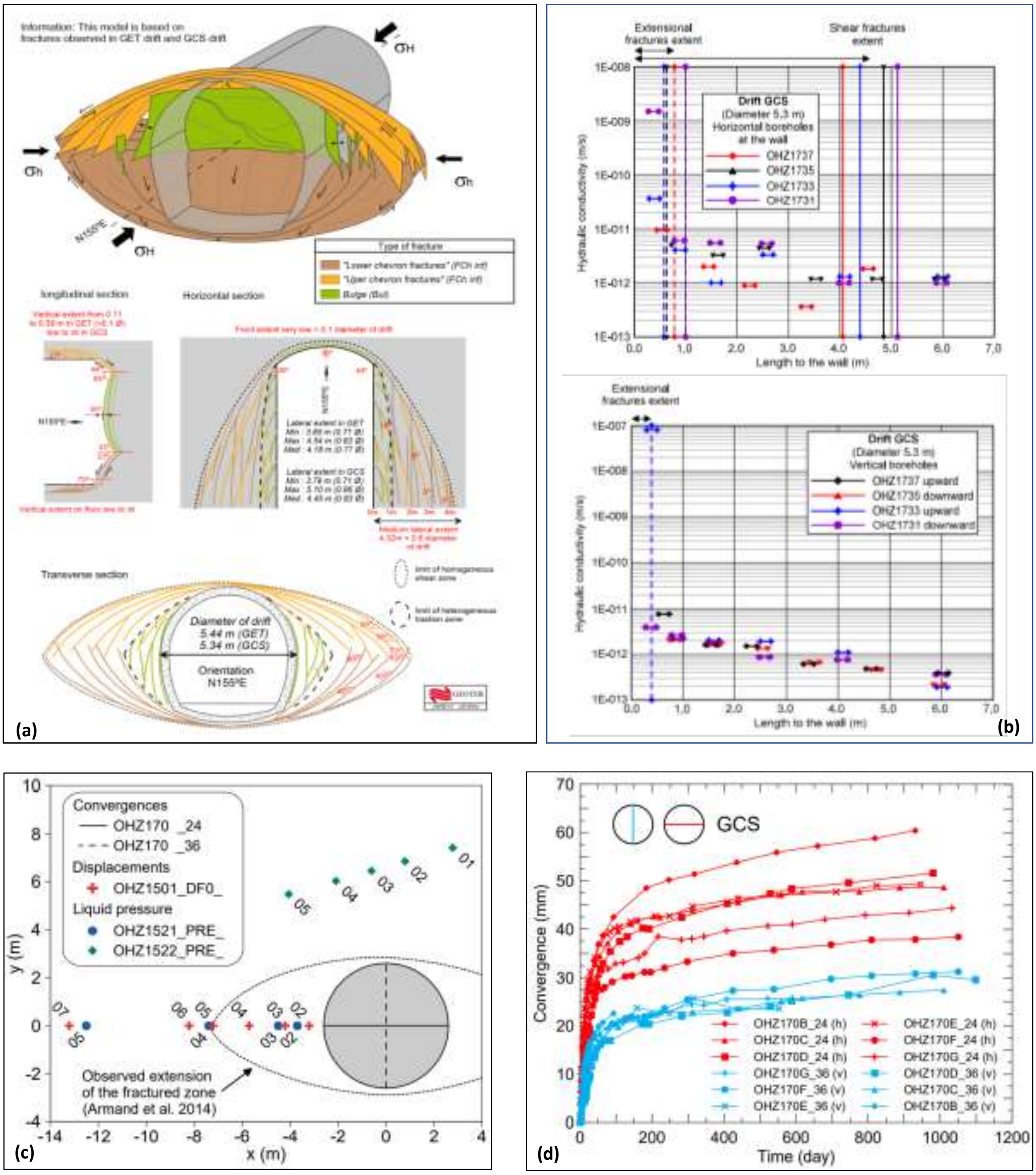

Figure 1 - In situ observations around the GCS drift, after Armand et al. (2014). (a) Conceptual model of the induced fractures network around a drift parallel to the major horizontal stress, (b) measured hydraulic conductivities with distance from the GCS drift wall along horizontal and vertical directions; (c) location of the in situ measurements around the GCS drift (displacements, pore pressure); (d) measured horizontal and vertical convergences

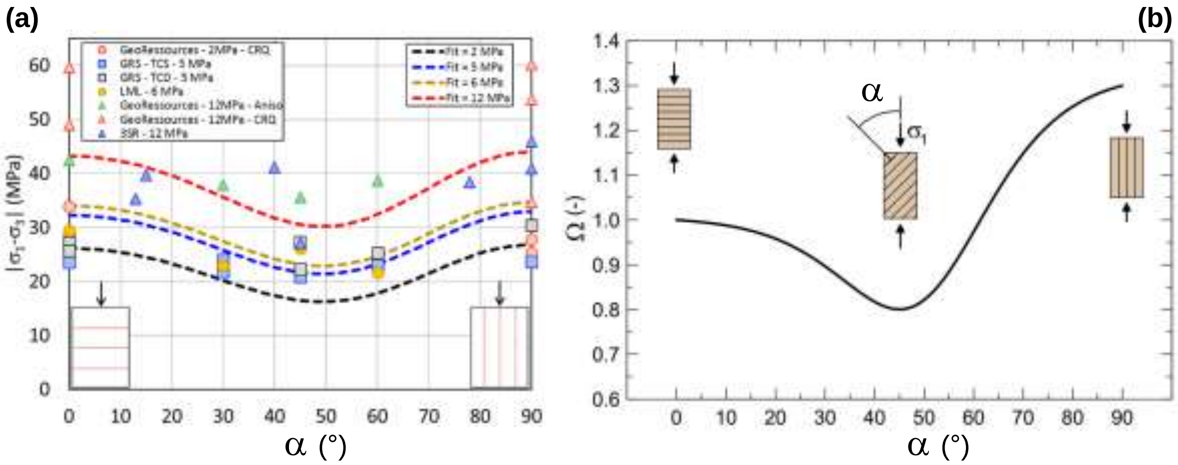

Figure 2 – (a) Synthesis of peak strength of COx claystone as function of the orientation of the major principal stress with respect to the bedding plane (Andra database) and a fitting with identical strengths at 0 and 90°, and minimum at 45°; (b) variation of cohesion and tensile strength with loading direction, relative to their reference value (after Manica et al. 2021)

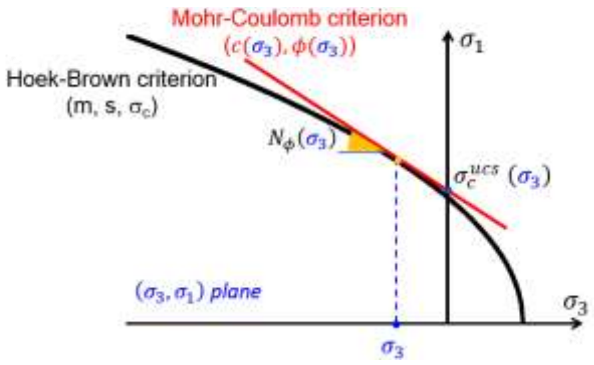

Figure 3 – Mohr-Coulomb criterion tangent to Hoek-Brown one at ⍰3

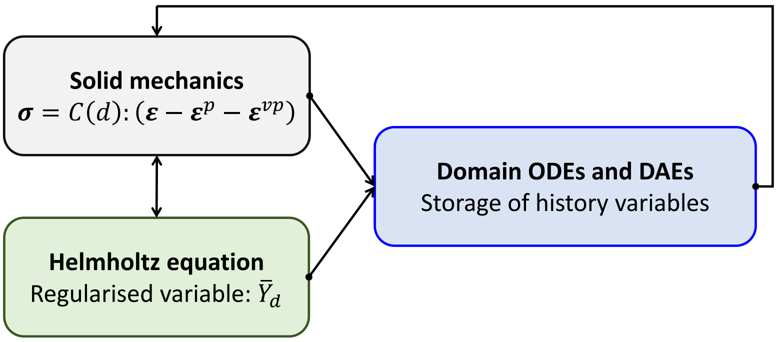

Figure 4 – Schematics of the Comsol implementation of the model using three modules

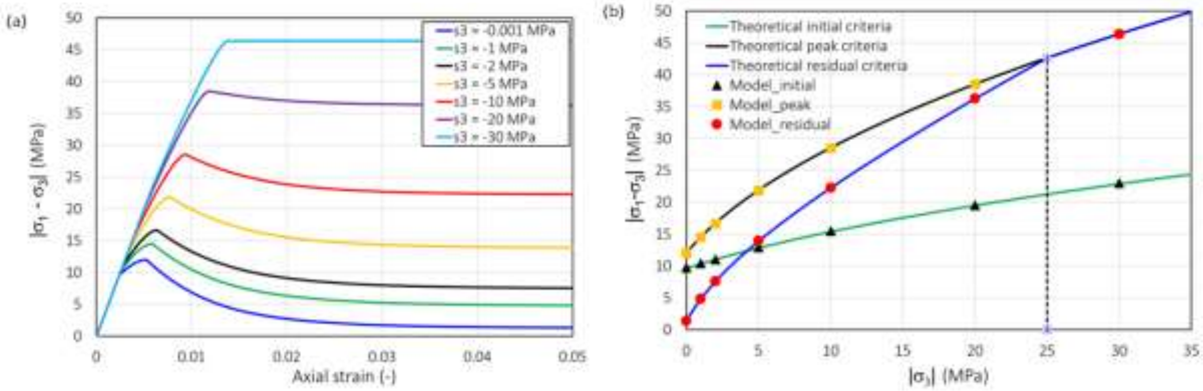

Figure 5 - Model verification on triaxial compression stress path for different confining pressure: (a) deviatoric stress vs axial strain curves and (b) elastic limit, peak, and residual strengths: numerical and theoretical solutions

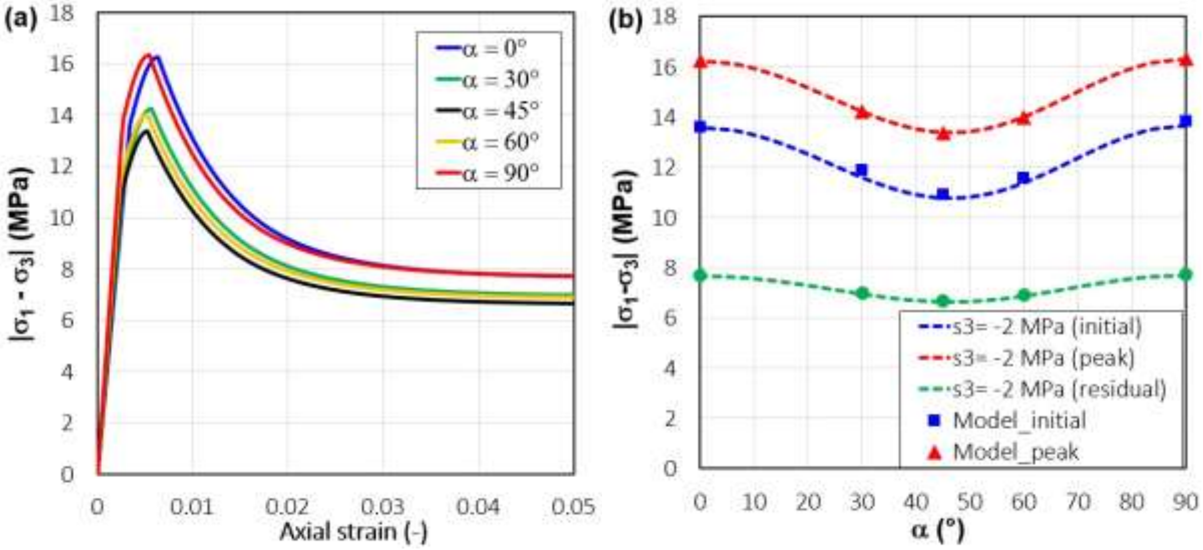

Figure 6 - Model verification for strengths anisotropy - triaxial compression for a confinement of -2 MPa and for different loading orientations with respect to the bedding: (a) deviatoric stress vs axial strain curves and (b) elastic limit, peak, and residual strengths: numerical and theoretical solutions, for a U-shaped strength evolution as the laboratory tests shown Figure 2**a**

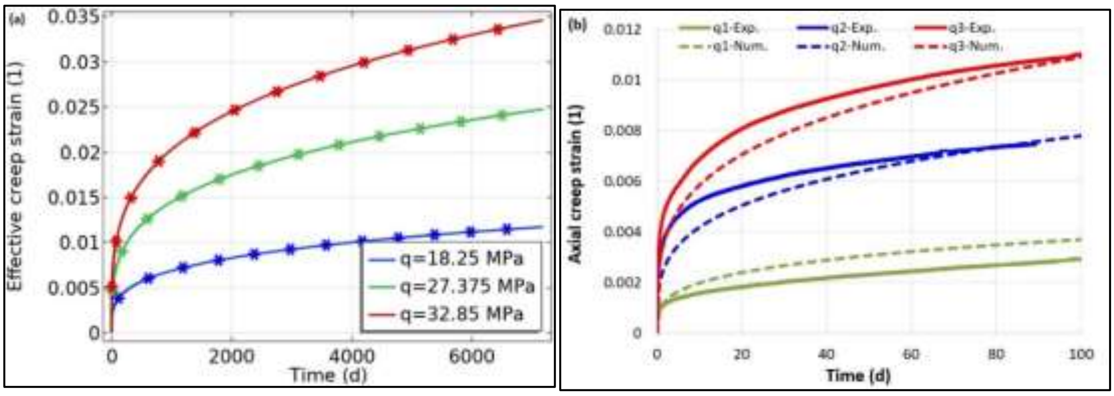

Figure 7- Creep tests on COx claystone: (a) comparison between the model (solid line) and the analytical expression eq. 16 (star); (b) comparison between the model and the creep tests of Armand et al. (2017)

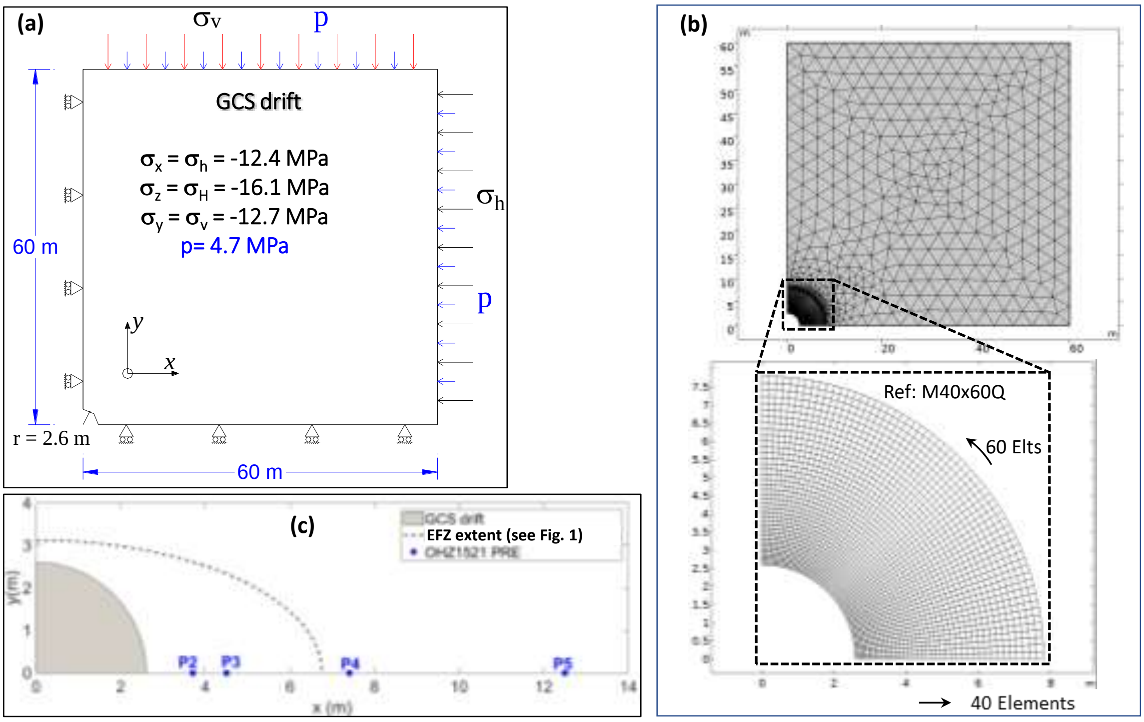

Figure 8 - (a) Geomechanical model of GCS drift, initial and boundary conditions; (b) finite element mesh used; (c) average observed EZF extent and location of pore pressure chambers in the borehole OHZ1521

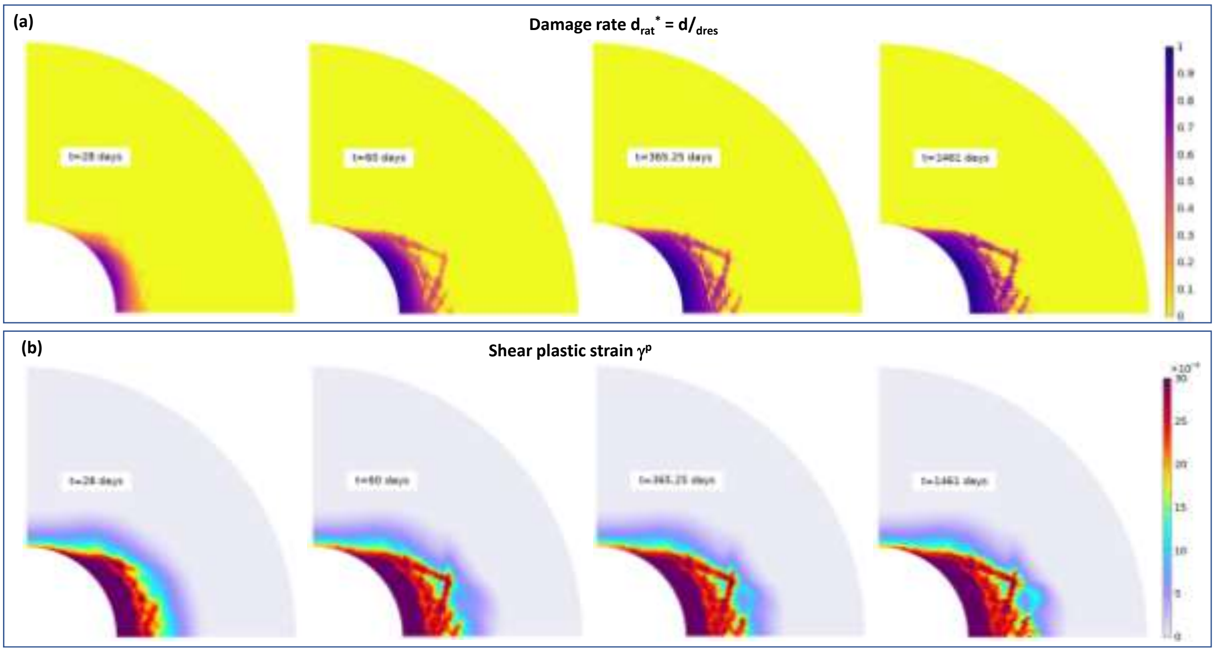

Figure 9 – Extent of damage rate (a) and plastic shear strain (b) at the end of excavation, 60 days, 1 year and 4 years

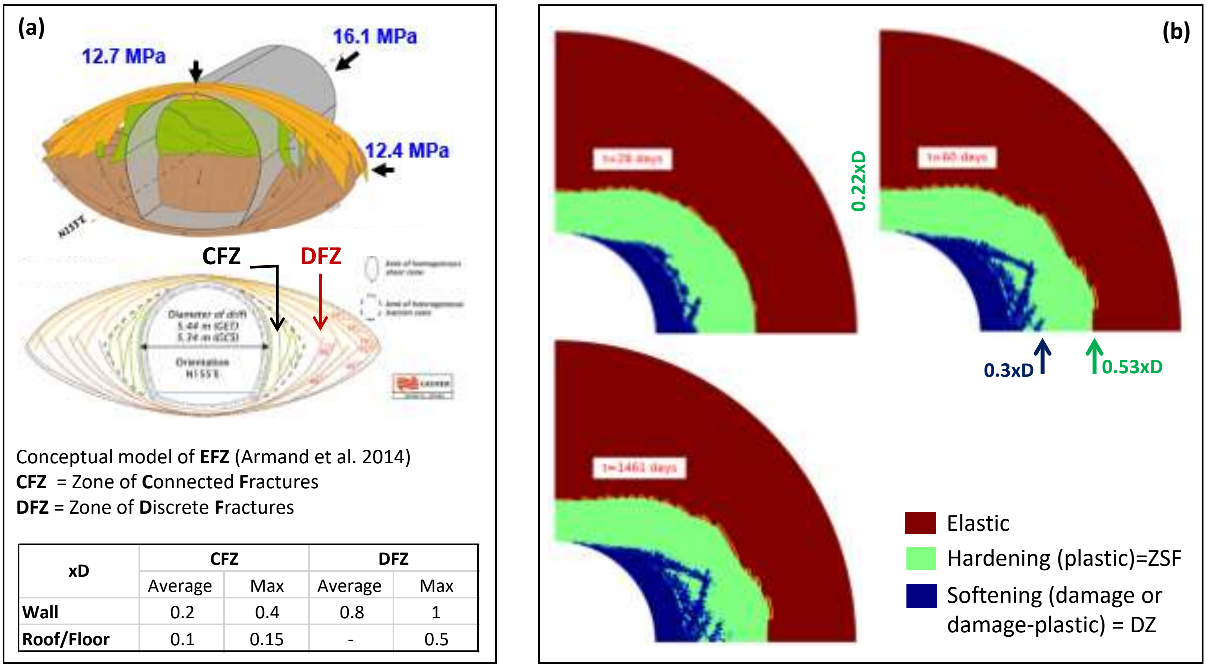

Conceptual model of **EFZ** (Armand et al. 2014)
CFZ = Zone of **C**onnected **F**ractures
DFZ = Zone of **D**iscrete **F**ractures

xD	CFZ		DFZ	
	Average	Max	Average	Max
Wall	0.2	0.4	0.8	1
Roof/Floor	0.1	0.15	-	0.5

Figure 10 – Excavation induced Fractured Zone (EFZ): (a) in situ observations (Armand et al. 2014), (b) numerical prediction

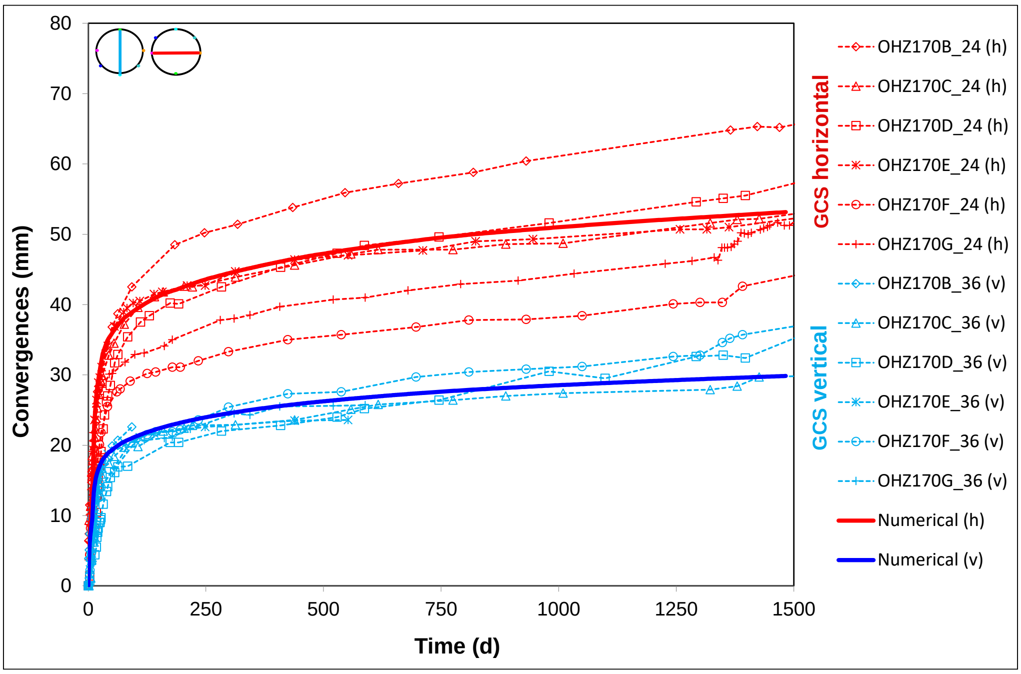

Figure 11 – Evolution of horizontal and vertical convergences around the GCS. Comparison between the field measurements and the numerical prediction

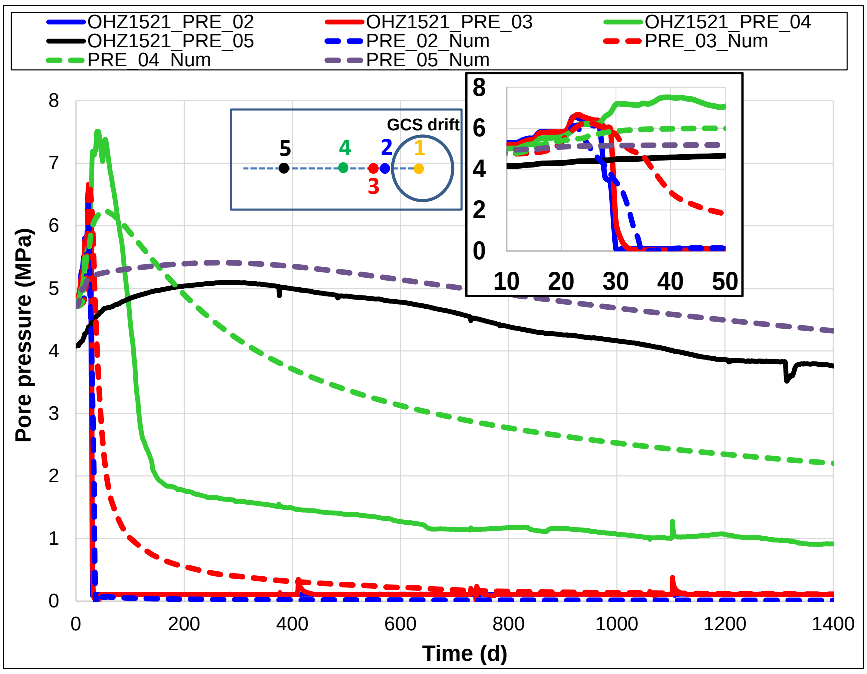

Figure 12 – Pore pressure measurements in the horizontal borehole OHZ1521: comparison with the numerical simulation

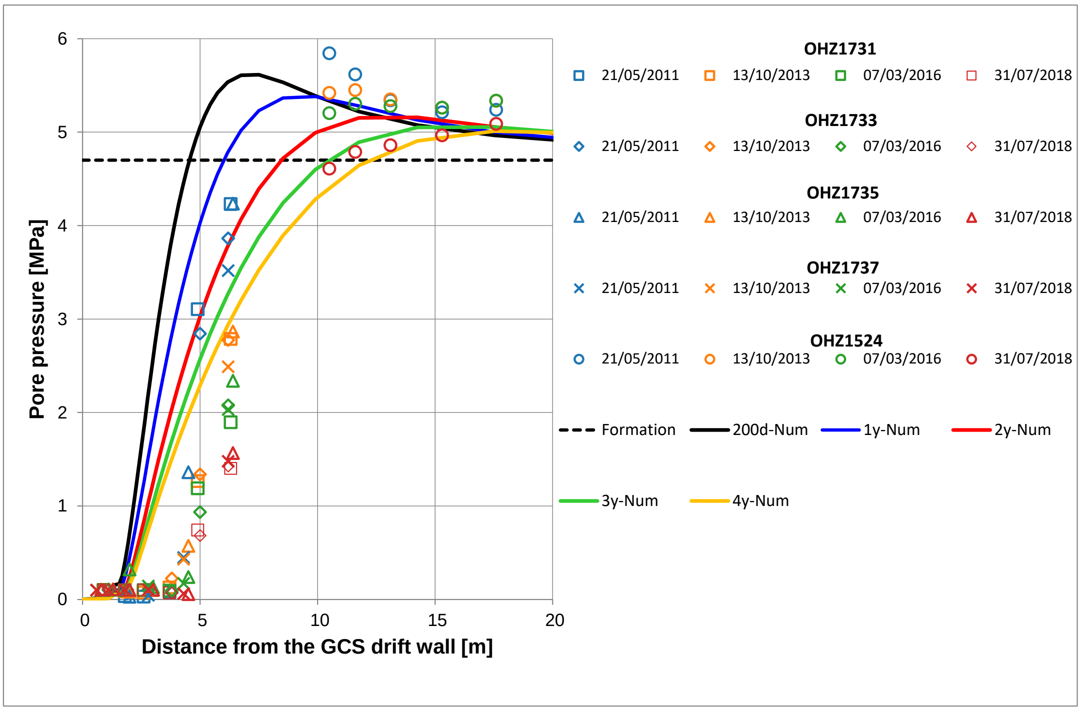

Figure 13 – Comparison of modelled and in situ measured pore pressure evolution along a radial profile of the GCS drift at different times

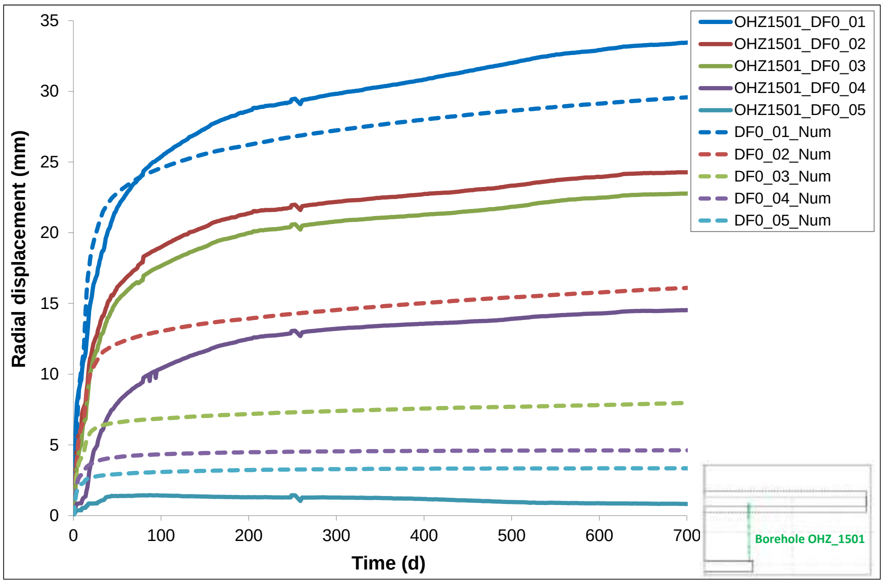

Figure14 – Variation in relative radial displacement (from the GCS wall) in rock mass along the borehole OHZ1501. Comparison with numerical simulation

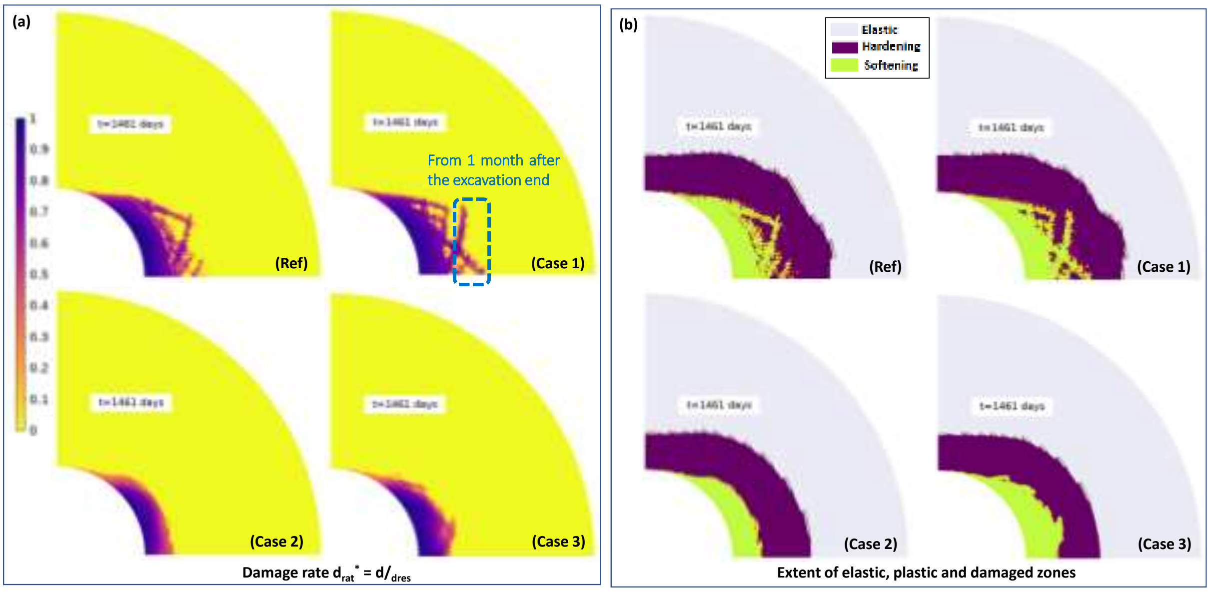

Figure 15 – Extent of damaged and plastic zones around GCS drift at 4 years. Sensitivity analysis on the effect of damage and shear failure on delayed deformations and permeability changes

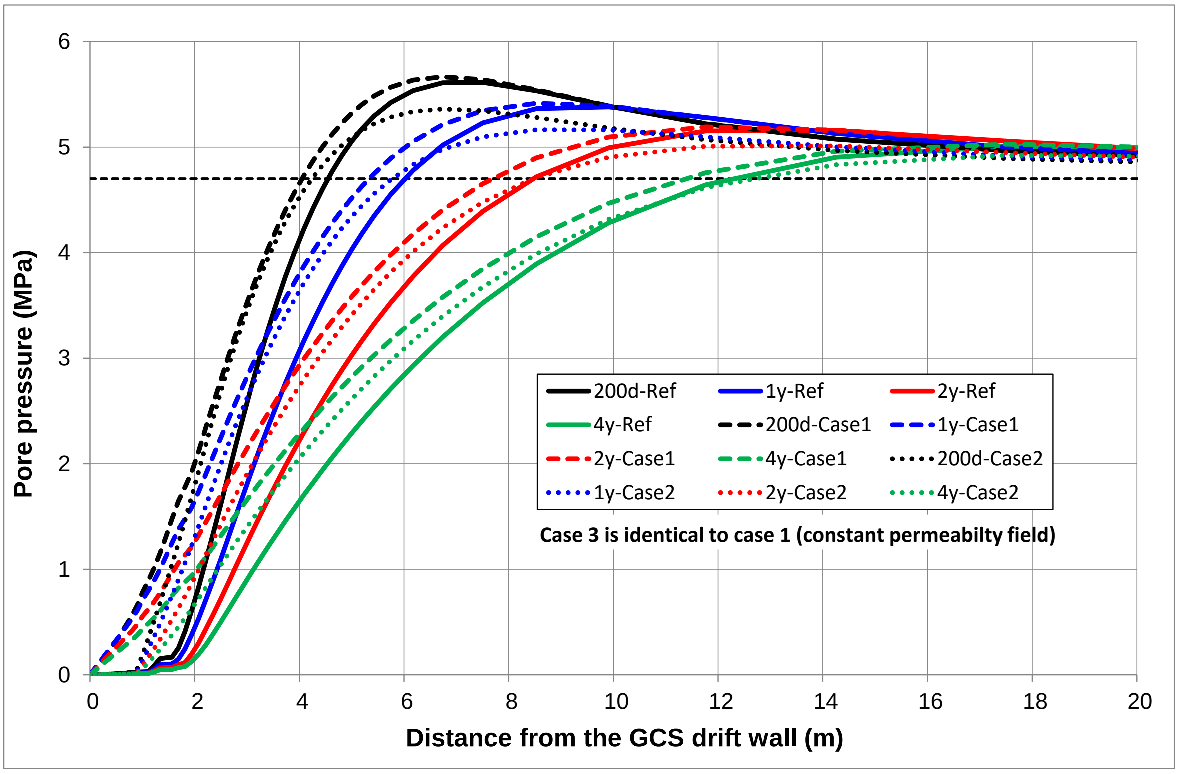

Figure 16 – Pore pressure evolution along the horizon profile for times 200 days, 1, 2 and 4 years. Sensitivity analysis on the effect of damage and shear failure on delayed deformations and permeability changes

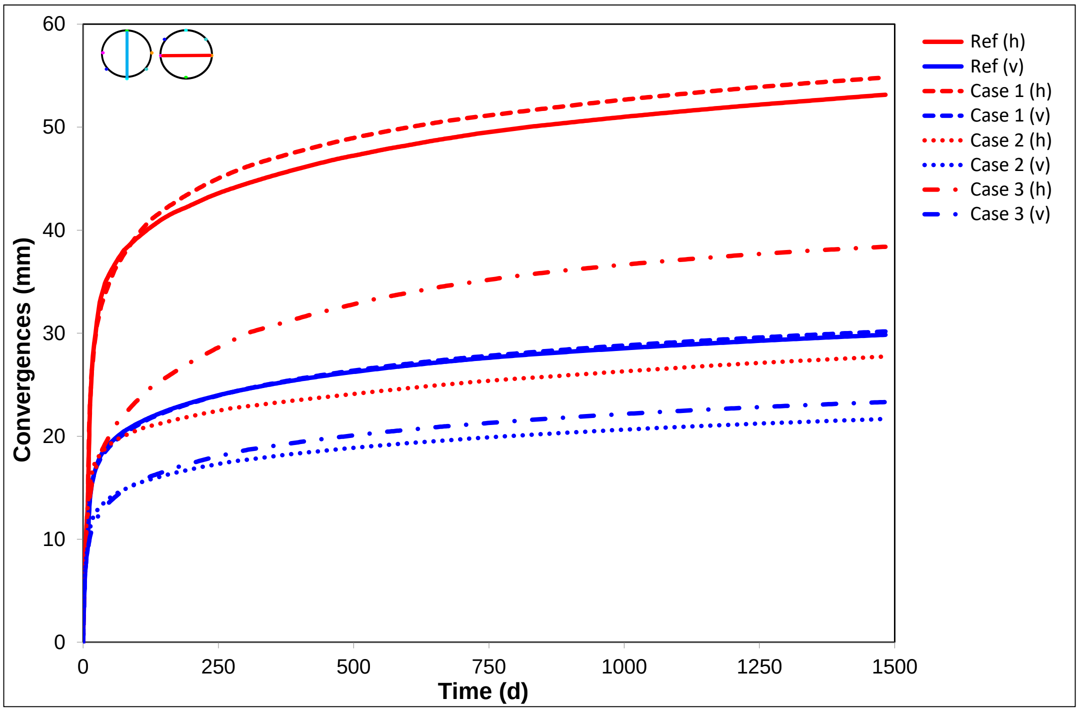

Figure 17 – Horizontal and vertical convergences around the GCS. Sensitivity analysis on the effect of damage and shear failure on delayed deformations and permeability changes

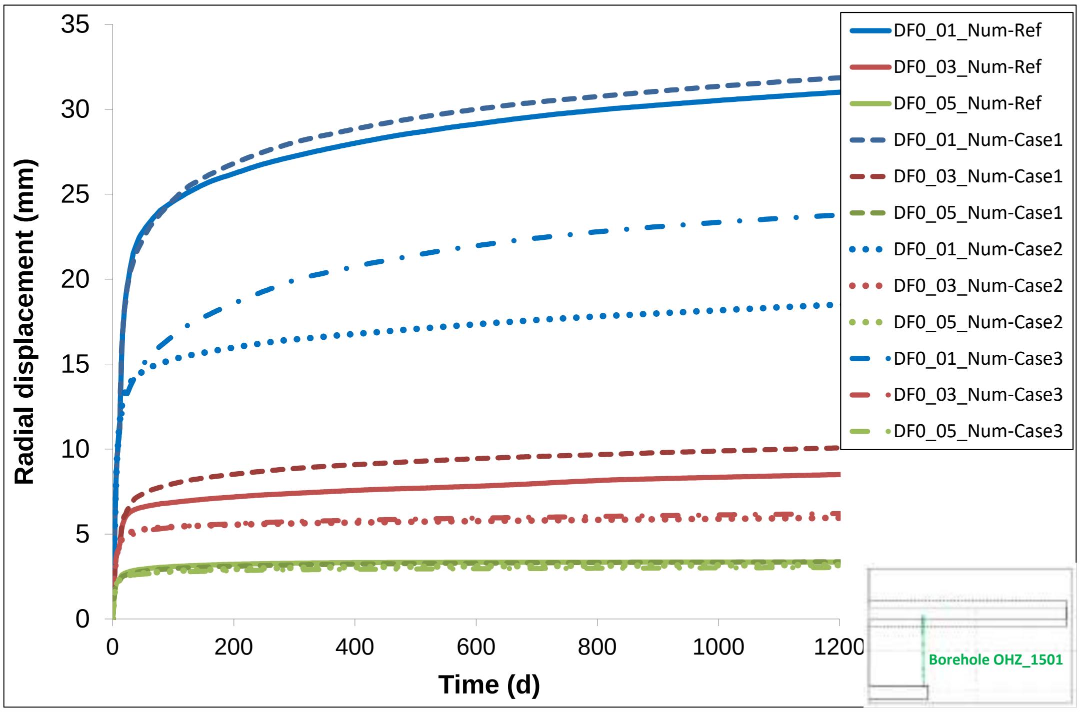

Figure 18 – Relative radial displacement (from the GCS wall) in rock mass along the borehole OHZ1501. Sensitivity analysis on the effect of damage and shear failure on delayed deformations and permeability changes

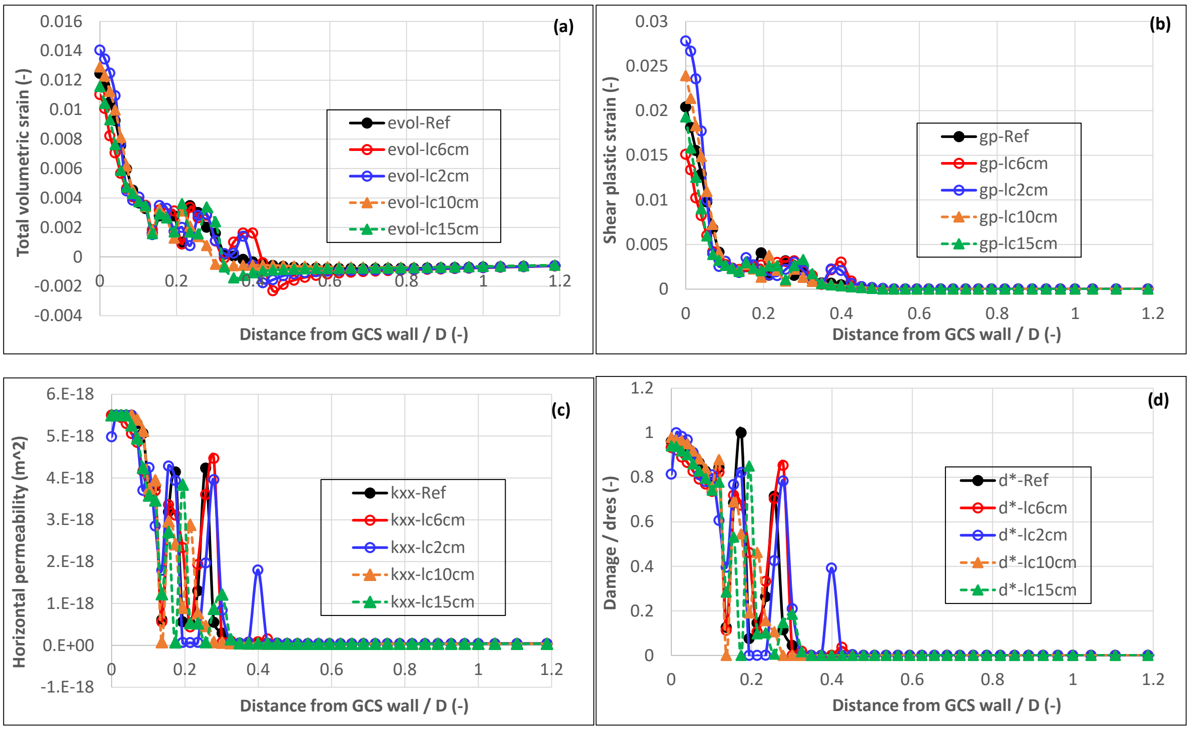

Figure 19 – Sensitivity analysis on the characteristic length $\left(l_{\gamma_p} = l_d = l_c\right)$. Distribution of (a) total volumetric strain; (b) plastic shear strain, γ_p; (c) intrinsic permeability in the plane of isotropy, $k_{//}$; (d) damage rate, $d_{rat}{}^{*}$, along the horizontal profile at the end of simulation (t = 1500 d). D is the GCS drift diameter

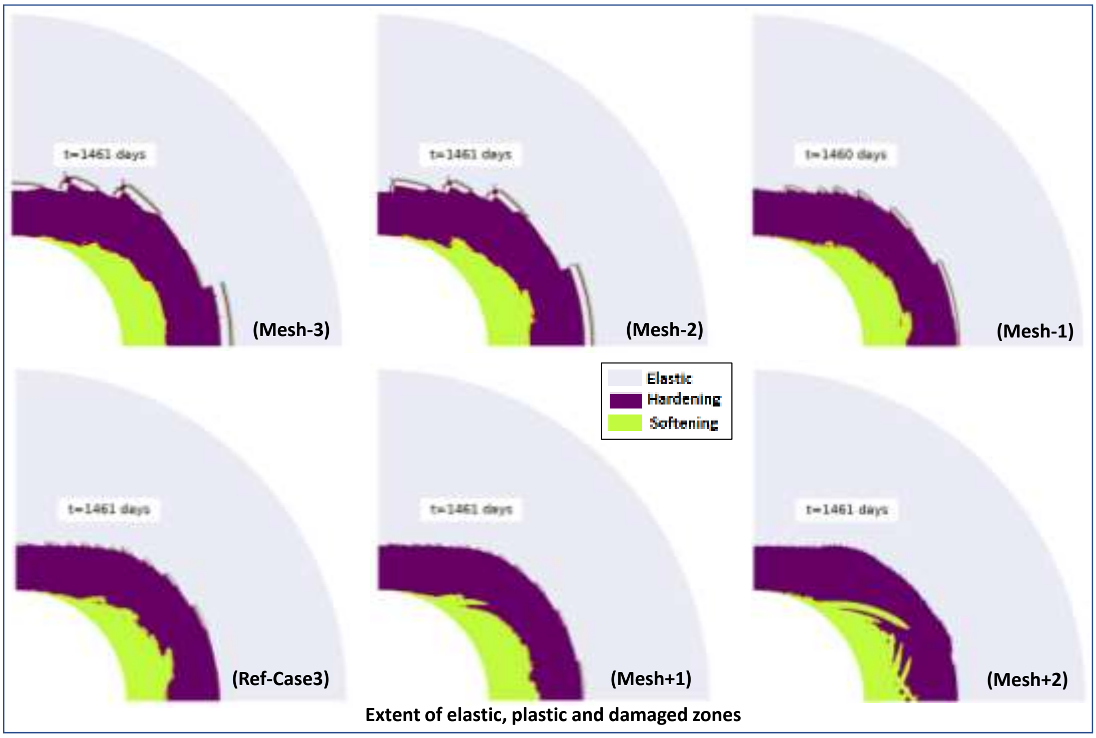

Figure A1 – Extent of damaged and plastic zones around GCS drift at 4 years. Effect of mesh size

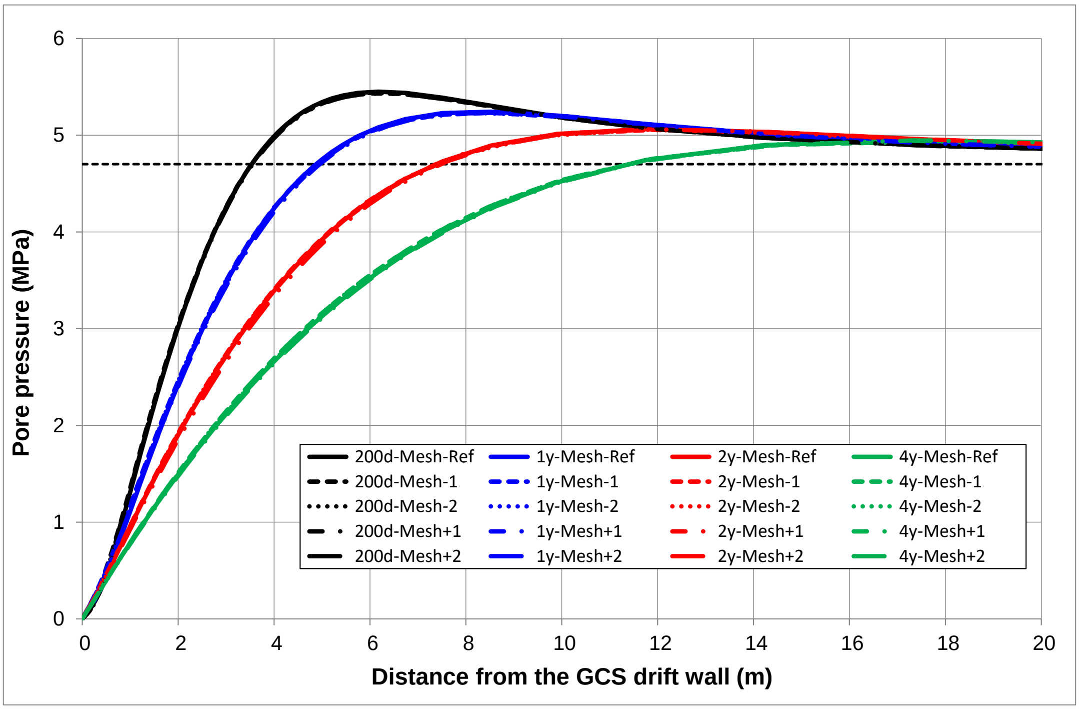

Figure A2 – Pore pressure evolution along the horizon profile. Effect of mesh size

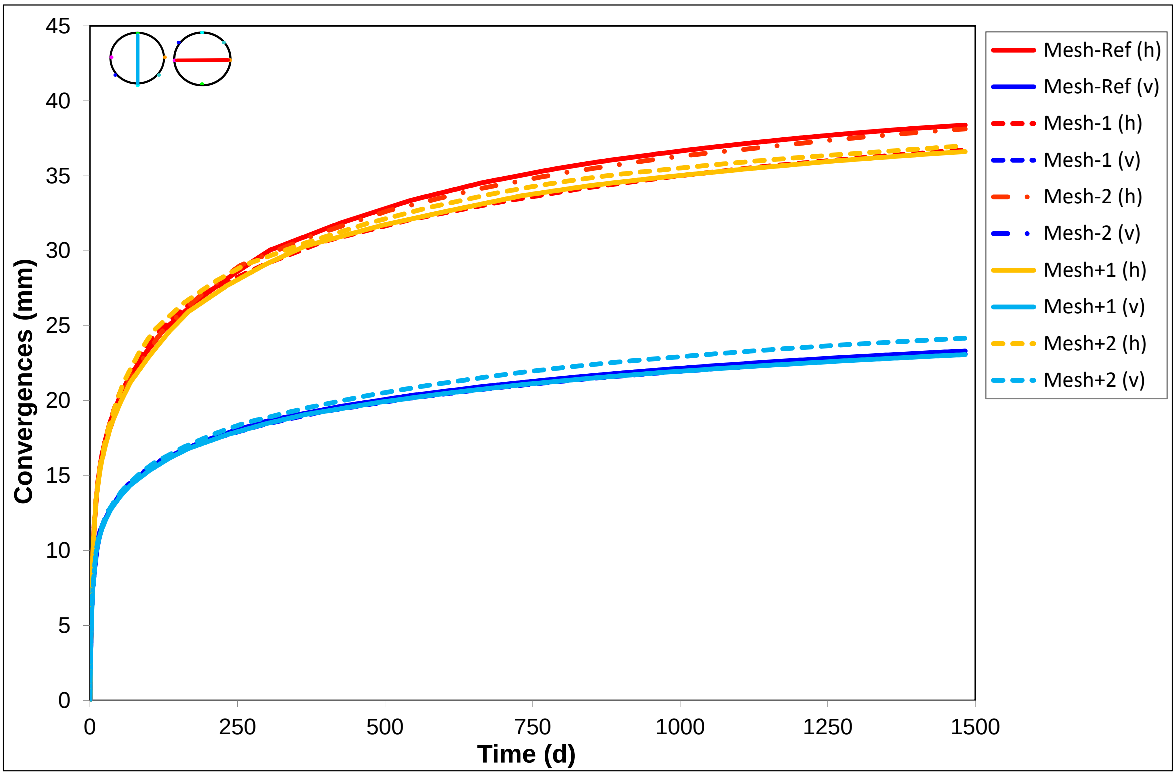

Figure A3 – Horizontal and vertical convergences around the GCS. Effect of mesh size

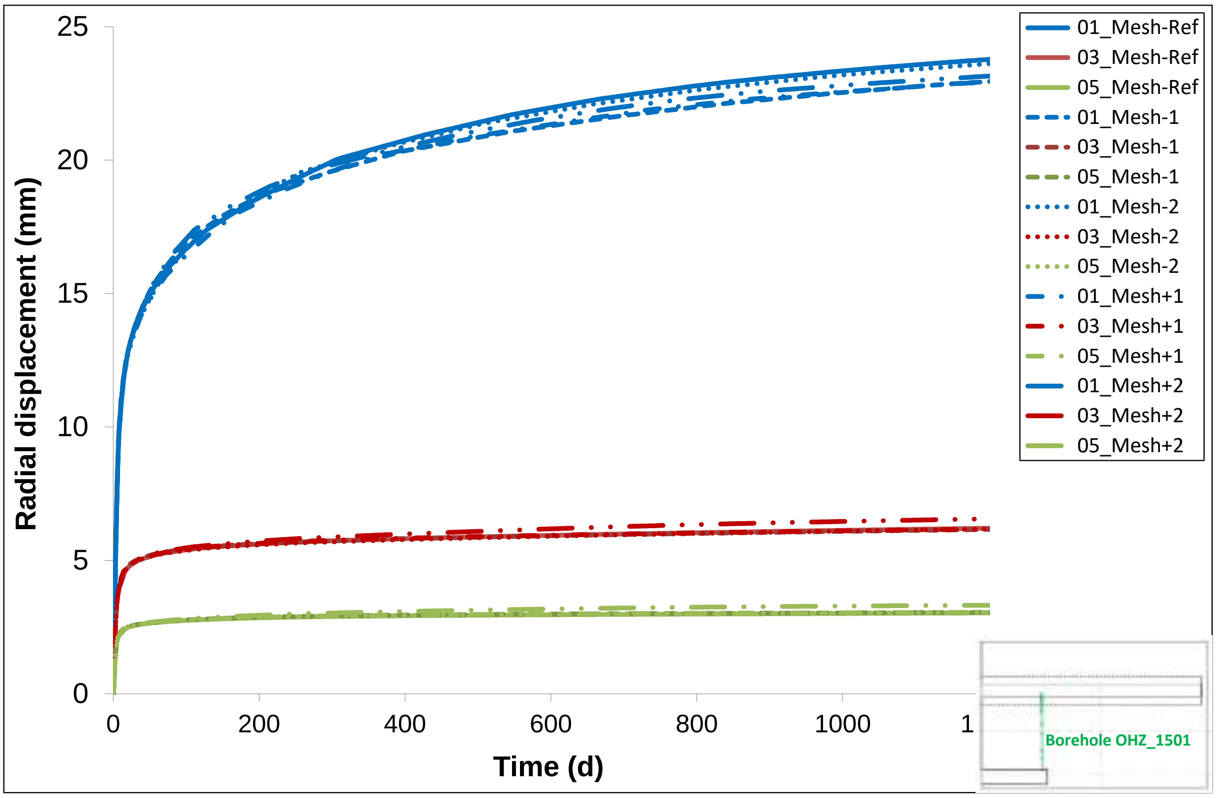

Figure A4 – Relative radial displacement (from the GCS wall) in rock mass along the borehole OHZ1501. Effect of mesh size